

A 3.5 Mpc-long radio relic in the galaxy cluster CIG 0217+70

D. N. Hoang¹, X. Zhang^{2,3}, C. Stuardi^{4,5}, T. W. Shimwell^{6,2}, A. Bonafede^{4,5}, M. Brüggen¹, G. Brunetti⁵, A. Botteon², R. Cassano⁵, F. de Gasperin^{1,5}, G. Di Gennaro^{2,8}, H. Intema², K. Rajpurohit⁴, H. J. A. Röttgering², A. Simionescu^{3,2,7}, and R. J. van Weeren²

¹ Hamburger Sternwarte, University of Hamburg, Gojenbergsweg 112, 21029 Hamburg, Germany
e-mail: hoang@hs.uni-hamburg.de

² Leiden Observatory, Leiden University, PO Box 9513, NL-2300 RA Leiden, The Netherlands

³ SRON Netherlands Institute for Space Research, Sorbonnelaan 2, 3584 CA Utrecht, The Netherlands

⁴ Dipartimento di Fisica e Astronomia, Università di Bologna, via Gobetti 93/2, 40122 Bologna, Italy

⁵ INAF - Istituto di Radioastronomia di Bologna, Via Gobetti 101, I-40129 Bologna, Italy

⁶ Netherlands Institute for Radio Astronomy (ASTRON), P.O. Box 2, 7990 AA Dwingeloo, The Netherlands

⁷ Kavli Institute for the Physics and Mathematics of the Universe (WPI), The University of Tokyo, Kashiwa, Chiba 277-8583, Japan

⁸ Harvard-Smithsonian Center for Astrophysics, 60 Garden Street, Cambridge, MA 02138, USA

Received xx 2021; accepted xx 2021

ABSTRACT

Context. Mega-parsec scale radio sources in the form of halos and relics are often detected in dynamically disturbed galaxy clusters and are generally thought to be generated merger-induced turbulence and shocks, respectively.

Aims. We aim to identify the mechanisms responsible for the particle acceleration and the magnetic field amplification in diffuse radio sources of the galaxy cluster CIG 0217+70.

Methods. We observed CIG 0217+70 with LOFAR at 141 MHz and VLA at 1.5 GHz, and combine with VLA 1.4 GHz archival data to study the morphological, spectral properties of the sources in the cluster. We add Chandra archival data to examine the thermal and non-thermal relation of the gas in the cluster centre.

Results. Our LOFAR and VLA new data confirm the presence of a giant radio halo in the cluster centre and multiple relics in the outskirts. The radio and X-ray emission from the halo are positively correlated, implying a tight relation between the thermal and non-thermal components. The SE radio structure with a projected size of 3.5 Mpc is the most extended radio relic detected to date. The spectral index across the width of the relics steepens towards the cluster centre, suggesting the energy ageing in the post-shock regions. The shock Mach numbers for the relics derived from the spectral index map reasonably range between 2.0 and 3.2. However, the integrated spectral indices lead to increasingly high Mach numbers for the relics farther from the cluster centre. This discrepancy could be because the relation between injection and integrated spectra does not hold for distant shocks, suggesting that the cooling time for the radio-emitting electrons is shorter than the crossing time of the shocks. The variations in the surface brightness of the relics and the low Mach numbers imply that the radio-emitting electrons are re-accelerated from fossil gas that is originally energised by active galactic nucleus activities.

Key words. Galaxies: clusters: individual: CIG0217+70 — Galaxies: clusters: intracluster medium — Large-scale structure of Universe — Radiation mechanisms: non-thermal — X-rays: galaxies: clusters

1. Introduction

Galaxy clusters reside at the intersection of cosmic filaments and grow through a series of mergers with smaller clusters/groups of galaxies. The merging of galaxy clusters (within a few Gyrs) converts an enormous amount of gravitational energy (i.e. up to 10^{64} ergs) into thermal and non-thermal energy. The former energy is in form of heating and compression the X-ray emitting plasma in the intra-cluster medium (ICM). The latter form of energy is channelled through the acceleration of cosmic rays and the amplification of magnetic fields. These events are the most energetic events in the Universe after the Big Bang (Sarazin 2002). During the mergers, shock waves and turbulence are generated in the ICM and are traced by diffuse radio synchrotron sources, namely radio halos and relics, respectively (see van Weeren et al. 2019 and Brunetti & Jones 2014 for recent reviews). Radio halos are steep-spectrum¹ ($\alpha \lesssim -1$), unpo-

larised, Mpc-scale sources that are detected at the cluster centre, whereas radio relics are steep-spectrum, highly-polarised at GHz frequencies, elongated sources that are normally detected in the cluster outskirts.

The favoured model for the formation of halos is the turbulent re-acceleration model in which mildly relativistic electrons ($\gamma \sim 10^2$ prior to the shock passage) in the cluster $\sim \mu\text{G}$ magnetic fields are re-accelerated by turbulence generated during mergers and emit synchrotron radiation (Brunetti et al. 2001; Petrosian 2001; Brunetti & Lazarian 2007, 2011, 2016; Pinzke et al. 2017). The relativistic electrons in relics were thought to be accelerated directly from the thermal pool at collisionless plasma shock fronts through Fermi-I Diffusive Shock Acceleration (DSA; Bell & R. 1978; Drury 1983; Blandford & Eichler 1987; Enßlin et al. 1998; Roettiger et al. 1999). Despite its success in explaining the observed properties (i.e. morphological, spectral and polarisation properties), the DSA model requires an acceleration efficiency that is unrealistically high to explain

¹ $S \propto \nu^\alpha$, where S is flux density at frequency ν and α is spectral index.

the observed surface brightness in some relics that are generated with low-Mach number shocks (i.e. $\mathcal{M} \approx 1.5 - 3$) (e.g. Hoeft et al. 2007; Vazza & Brüggen 2014; Botteon et al. 2020a). An alternative Diffusive Shock Re-Acceleration (DSRA) model where a population of mildly relativistic fossil plasma is required to be present prior to the (re-)acceleration by the passage of the low-Mach number shocks has been proposed to solve this energy problem (Markevitch et al. 2005; Kang & Ryu 2011; Kang et al. 2012). There has been observational evidence for this re-acceleration scenario in some clusters (e.g. van Weeren et al. 2013; Bonafede et al. 2014; Shimwell et al. 2015; Botteon et al. 2016; van Weeren et al. 2017; Hoang et al. 2018; Gennaro et al. 2018; Stuardi et al. 2019).

The galaxy cluster CIG0217+70 (hereafter CIG0217; $z = 0.18$, Zhang et al. 2020) was studied with the Very Large Array (VLA) at 1.4 GHz and 325 MHz by Brown et al. (2011) after the first detection with the Westerbork Northern Sky Survey (WENSS; Rengelink et al. 1997; Delain & Rudnick 2006; Rudnick et al. 2006). Brown et al. (2011) found that the cluster hosts multiple radio diffuse sources including a radio halo, double relics on opposite sides of the cluster, and internal filaments. The elongation of the X-ray emission in the ROSAT All-Sky Survey (RASS) image suggests its merger state. They analysed the photometric redshifts from galaxies in the field using the Sloan Digital Sky Survey (SDSS) optical data and found that the cluster has a redshift of $z = 0.0655$, but also suggested the need of deeper optical data to verify the result. With this low-redshift estimate, Brown et al. (2011) pointed out that the power of the radio halo in CIG0217 is an order of magnitude higher than the predicted value from the radio power–X-ray luminosity correlation (Liang et al. 2000; Cassano et al. 2006; Brunetti et al. 2009). However, recent work by Zhang et al. (2020) estimated a significantly higher redshift for the cluster, i.e. $z = 0.18$, from the Fe xxv He α X-ray emission line that they detected in *Chandra* archival data. Using this new redshift, they found that the power of the radio halo increases by an order of magnitude. They also estimated the mass of the cluster to be $M_{500} = (1.06 \pm 0.11) \times 10^{15} M_{\odot}$ using the $M_{500} - kT$ scaling relation (Arnaud et al. 2007), making this cluster one of the most massive clusters. At the locations of the northern and southern radio halo edges, they found discontinuities in the X-ray surface brightness (SB) with density jumps of $C_N = 1.40 \pm 0.16$ and $C_S = 3.0 \pm 0.6$, respectively. The radio emission at 1.4 GHz is found to have a steep SB slope at the location of the northern X-ray SB jump. Due to the low integration time of X-ray observations, it is not clear whether the discontinuities are caused by shock or cold fronts.

In this paper, we present LOw Frequency ARray (LOFAR; Haarlem et al. 2013) 120–168 MHz observations of CIG0217 to study the diffuse radio emission from the cluster at low frequencies. We combined the LOFAR data with the VLA L-band C- and D-array archival data to examine the spectral properties of these sources. We did not include the relatively shallow VLA P-band data reported in Brown et al. (2011) to this study. In addition, *Chandra* X-ray archival data was used for examining the correlation between X-ray thermal and radio non-thermal emission from the diffuse sources in the cluster. Throughout the paper, we assume a Λ CDM cosmology with $\Omega_M = 0.3$, $\Omega_{\Lambda} = 0.7$, and $H_0 = 70 \text{ km s}^{-1} \text{ Mpc}^{-1}$. At the cluster redshift ($z = 0.18$), an angular scale of $1'$ then corresponds to a physical size of 182 kpc.

2. Observations and data reduction

2.1. LOFAR data

LOFAR High Band Antenna (HBA) observations of CIG0217 were performed on September 26, 2018 (project code: LC10_021). The observation settings are identical to those used by the LOFAR Two-metre Sky Survey (LoTSS; Shimwell et al. 2017, 2019). The 8-hour observation of the target field was book-ended by 10-minute scans of calibrators (i.e. 3C 196 and 3C 48). The observations were performed with core and remote stations in the Netherlands and international stations in surrounding European countries. The distance between the Dutch stations that are used in this study ranges from 42 m to 115 km, corresponding to 20λ to $61k\lambda$ at the central frequency of 141 MHz. The high-density of the LOFAR core stations makes it highly sensitive to diffuse sources. Details of the observations are given in Tab. 1.

The calibration of the LOFAR data was performed using the standard pipelines (i.e. Prefactor² and DDF – pipeline³) that have been developed for the LOFAR Surveys Key Science Project (van Weeren et al. 2016b; Shimwell et al. 2017, 2019; de Gasperin et al. 2019; Tasse et al. 2021). The pipelines address the direction-dependent and direction-independent effects that are commonly known to affect low-frequency radio observations. Following the direction dependent calibration, all sources outside a square region of $1 \times 1 \text{ deg}^2$ centred on the cluster were subtracted from the uv data. This subtracted data was then processed through several iterations of self-calibration to refine the image quality at the location of the target (van Weeren et al. 2020). We note that the data was applied an approximate correction for the LOFAR primary beam attenuation by multiplication with a factor during the subtraction step. However, as the pointing position is at the location of the cluster, the factor is 1. Due to the large angular distance of the sources to the pointing centre of CIG0217 (i.e. up to $15'$), the flux densities of these sources were not properly corrected. We additionally applied the primary beam correction during the final imaging steps below that results in up to 15% increase in the flux density for the sources in the cluster outskirts. To enhance faint, diffuse emission in the final images, we applied Briggs' weightings of the uv data using various robust values (see Tab. 2) with WSCLEAN (version 2.9.3; Offringa et al. 2014; Offringa & Smirnov 2017). We also used joined-channel and multi-scale deconvolution (Offringa & Smirnov 2017) with the `join-channels` (`channels-out=6`) and `multiscale` (`multiscale-scales=[0, 3, 7, 25, 60, 150]`) options. The built-in option `apply-primary-beam` was added in the CLEAN command to correct for the response of the LOFAR primary beam across the imaged region.

We examine the flux scale of the LOFAR images by comparing the flux densities of compact sources in our LOFAR images with those detected with the TIFR GMRT 150 MHz Sky Survey-Alternative Data Release (TGSS-ADR1; Intema et al. 2017). We selected compact sources that are brighter than 100 mJy and were detected with both the LOFAR and TGSS-ADR1 observations. The average flux densities for these sources in our LOFAR image are about 5 percent higher than those in the TGSS-ADR1 image. In this paper, we adopt a flux scale uncertainty of 10 percent on the LOFAR data as assumed by a number of previous studies (e.g. Bruno et al. 2021; Rajpurohit et al. 2021).

² <https://www.astron.nl/citt/prefactor>

³ <https://github.com/mhardcastle/ddf-pipeline>

Table 1: Observation details

Telescope	LOFAR 141 MHz	VLA 1.4 GHz	VLA 1.5 GHz
Project	LC10_021	AD509	17A-083
Configuration	HBA_DUAL_INNER	D	C
Pointing position	02 ^h 17 ^m 1.4 ^s , +70 ^d 36 ^m 16.0 ^s	02 ^h 17 ^m 0.0 ^s , +70 ^d 36 ^m 36.0 ^s	02 ^h 18 ^m 49.9 ^s , +70 ^d 27 ^m 36.0 ^s (E); 02 ^h 14 ^m 31.0 ^s , +70 ^d 41 ^m 04.0 ^s (W)
(R.A., Dec.)			
Observing dates	2018 Sept. 26	2005 Dec. 4, Dec. 8, Dec. 12	Jun. 3, 2017
Obs. IDs	L670298	–	–
Calibrator(s)	3C 196	3C 286, 3C 352, 0217+738	3C 138, J0217+7349
Frequency (GHz)	0.120 – 0.168	1.37 – 1.48	1.008 – 2.032
Number of subbands	243	–	16
Bandwidth per subband (kHz)	195.3	–	64000
Channels per subband	16	–	64
On-source time (hr)	8	3.5	1.7 (E) + 1.7 (W)
Integration time (s)	1	13	5
Frequency resolution (kHz)	12.2	12.5	1000
Correlations	XX, XY, YX, YY	RR, LL	RR, RL, LR, LL
Number of stations/antennas	60	23	27

Table 2: Imaging parameters.

Data	uv -range [kλ]	Robust ^a	uvtaper [′′]	θ_{FWHM} [′′×′′], (PA^b [°])	σ_{rms} [μJy beam ⁻¹]	Fig.	Notes
LOFAR	0.12 – 61	0	5	14.6 × 10.1 (–85)	160	6	intensity
	0.12 – 61	0	15	26.6 × 22.5 (29)	240	2, 6	intensity
	0.12 – 61	0.25	25	45.7 × 44.7 (52)	335	2, 4	intensity
	0.12 – 61	0	30	46 × 46 ^c	345	7	spectral index
	0.12 – 61	0	5	16 × 16 ^c	190	7	spectral index
	2 – 61	–0.25	5	11.2 × 7.5 (–89)	140	1	beam uncorrected
VLA (C-array)	0.12 – 22	0	8	16 × 16 ^c	40	7	spectral index
VLA (D-array)	0.12 – 5.1	0	–	46 × 46 ^c	85	7	spectral index
	2.0 – 5.1	–2	–	28.4 × 24.6 (51)	80	1	beam uncorrected

Notes: ^a: Briggs weighting, PA : position angle with the reference axis to the north and counter-clockwise as positive, ^c: smoothed.

2.2. VLA data

We observed ClG0217 with the VLA L-band in C array on June 3, 2017 (Project: 17A-083) and combine with archival data obtained with the D array between December 4 and 12, 2005 (Project: AD509). Details of these observations are summarized in Tab. 1.

The VLA L-band C-array observations were performed using two pointings centred 13′ to the north-west and to the south-east of the centre of the cluster. This was done to avoid the attenuation due to the antenna primary beam in the peripheral regions of the cluster. We processed the data using the VLA CASA calibration pipeline version 4.7.2. The processing was optimized with the additional flagging and calibration to produce high-quality images. 3C 138 was used as amplitude and band-pass calibrator; and J0217+7349 was used for a phase calibration. After the initial imaging, several cycles of self-calibration were separately performed on the two pointings in order to refine the calibration. Finally, we make use of the `tclean` task in CASA (version 5.6; McMullin et al. 2007) to separately make intensity images for two pointings. A wideband correction for the primary beam attenuation using `widebandpbcor` was applied to the images. We then combined the images to make a mosaic of the cluster. The pixel values in the overlay regions between the pointings where the amplitude of the primary beams are larger than 0.2 were averaged, weighted by their amplitude.

We reprocessed the VLA L-band D-array data sets that were originally presented in Brown et al. (2011). The data was calibrated using CASA (version 5.6; McMullin et al. 2007). The flux densities of the sources are calibrated using observations of 3C 286 and 3C 352 that we tied to the Perley & Butler (2017) flux scale. The compact source 0217+738, which is located approximately 3 degree from ClG0217, was observed in between target scans and was used as a phase calibrator. The calibration was performed for each data set in a standard manner (i.e. flagging of outliers, calibrating of the flux scale, antenna position, phase delay, bandpass, and complex gain). After the initial calibration, the data sets were combined and processed through multiple loops of self-calibration. The final calibrated data was used to make images of the cluster at different resolutions using Briggs’ weightings with various tapering values of the uv data. Final images were also corrected for the attenuation of the primary beam (i.e. by using `pbcor=True` option in `tclean`). We adapted a flux scale uncertainty of 5 percent associated with the calibration of the VLA data. We note that due to the different settings (i.e. pointing positions) of the VLA C-array and D-array observations we do not combine the data sets for final imaging.

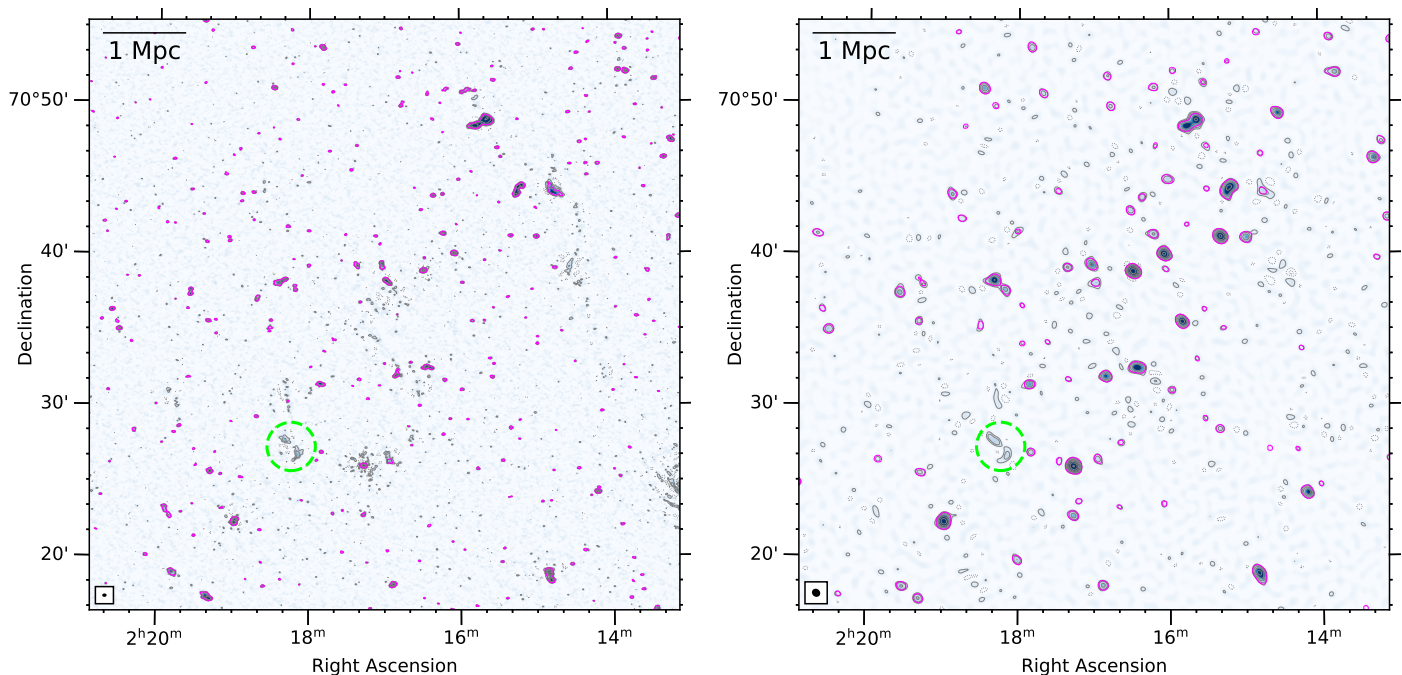


Fig. 1: LOFAR 141 MHz (*left*) and VLA 1.4 GHz (*right*) high-resolution flat-noise images (i.e. primary beam uncorrected). The contaminating discrete sources that are marked with the magenta contours and are removed from the uv data. The source in the dashed circle is not included in the subtracted model. The contours are $[1, 2, 4, 8, 16] \times 3\sigma$, where $\sigma_{\text{LOFAR}} = 140 \mu\text{Jy beam}^{-1}$ and $\sigma_{\text{VLA}} = 80 \mu\text{Jy beam}^{-1}$.

2.3. Removal of discrete sources

The diffuse sources in CIG0217 are contaminated by discrete sources which we removed from the LOFAR and VLA D-array uv data by subtracting their models. The removal of the discrete sources is essential for studying the flux density and spectra of the diffuse sources. To perform the removal of discrete sources, their models at 141 MHz and 1.4 GHz were created by imaging the data at high resolutions using only the baselines longer than $2 k\lambda$ (i.e. corresponding to an angular size of $< 2.1'$ or $< 382 \text{ kpc}$ at $z=0.18$) and applying Briggs' weighting to give more weight to the long baselines (i.e. $\text{robust} = -0.25$ for LOFAR and $\text{robust} = -2$ for VLA). An advantage of the combination of these settings is that they prevented any significant large-scale emission from being present in the model images which is subtracted from the data. Moreover, when including more data for imaging, the noise level of the model images is lowered which allows the detection of faint, compact sources. In Fig. 1 we show the LOFAR and VLA images that are obtained with these imaging parameters that were tuned to show just the compact sources in the field of CIG0217, but the diffuse emission from CIG0217 is not clearly seen. The discrete sources shown with magenta contours in Fig. 1 are identified with PyBDSF using source detection threshold of 4σ (i.e. $\text{thresh_pix} = 4$). These clean component models of the contaminating sources were then subtracted from the LOFAR and VLA uv data.

2.4. Spectral index maps

We combined the LOFAR 141 MHz data with the VLA 1.4 GHz (D-array) and 1.5 GHz (C-array) data to make spectral index maps of the radio sources in the cluster field. When making the LOFAR and VLA images, we selected the uv data with a common inner uv cut for both data sets. Here we used a inner uv cut of $0.12 k\lambda$ for the $16''$ and $46''$ resolution maps. Briggs' weight-

ing of the uv data ($\text{robust} = 0$) is combined with tapering of the outer baselines (uvtaper) to obtain images with the resolutions that are close to the targeted resolutions (i.e. $16''$ and $46''$). The imaging of the LOFAR and VLA data were done with WSClean and CASA, respectively (see Sec. 2.1 and 2.2). The LOFAR and VLA images were smoothed to the final resolutions, aligned using compact sources, and regridded to the same pixel size. The properties of the final images are given in Tab. 2. Spectral index maps were made with the LOFAR and VLA final images, following the power-law relation of the synchrotron spectrum. The spectral index errors are added in quadrature from the flux scale uncertainty and the image noise.

3. Results

In Fig. 2 we present the LOFAR 141 MHz contour image of the galaxy cluster CIG0217 overlaid on the Sloan Digital Sky Survey (SDSS) optical (r, g, and i bands) image (Alam et al. 2015). The LOFAR data confirms the presence of diffuse radio emission in the cluster central region (i.e. source A) and elongated radio sources (i.e. source B, C, D, E, F, and G) in the outskirts that were detected at 1.4 GHz with the VLA observations by Brown et al. (2011).

3.1. Central diffuse source

3.1.1. Flux density and spectral measurements

The presence of the diffuse radio emission (i.e. source A) at the centre of CIG0217 is clearly seen in the LOFAR and VLA images in Figs. 2, 4, and 5. The source was identified as a giant radio halo by Brown et al. (2011). At 141 MHz the radio halo roughly has a round shape and is more extended with a projected diameter of 1.8 Mpc than that measured at 1.4 GHz (i.e. 1.5 Mpc). The size of the halo at 1.5 GHz is significantly smaller,

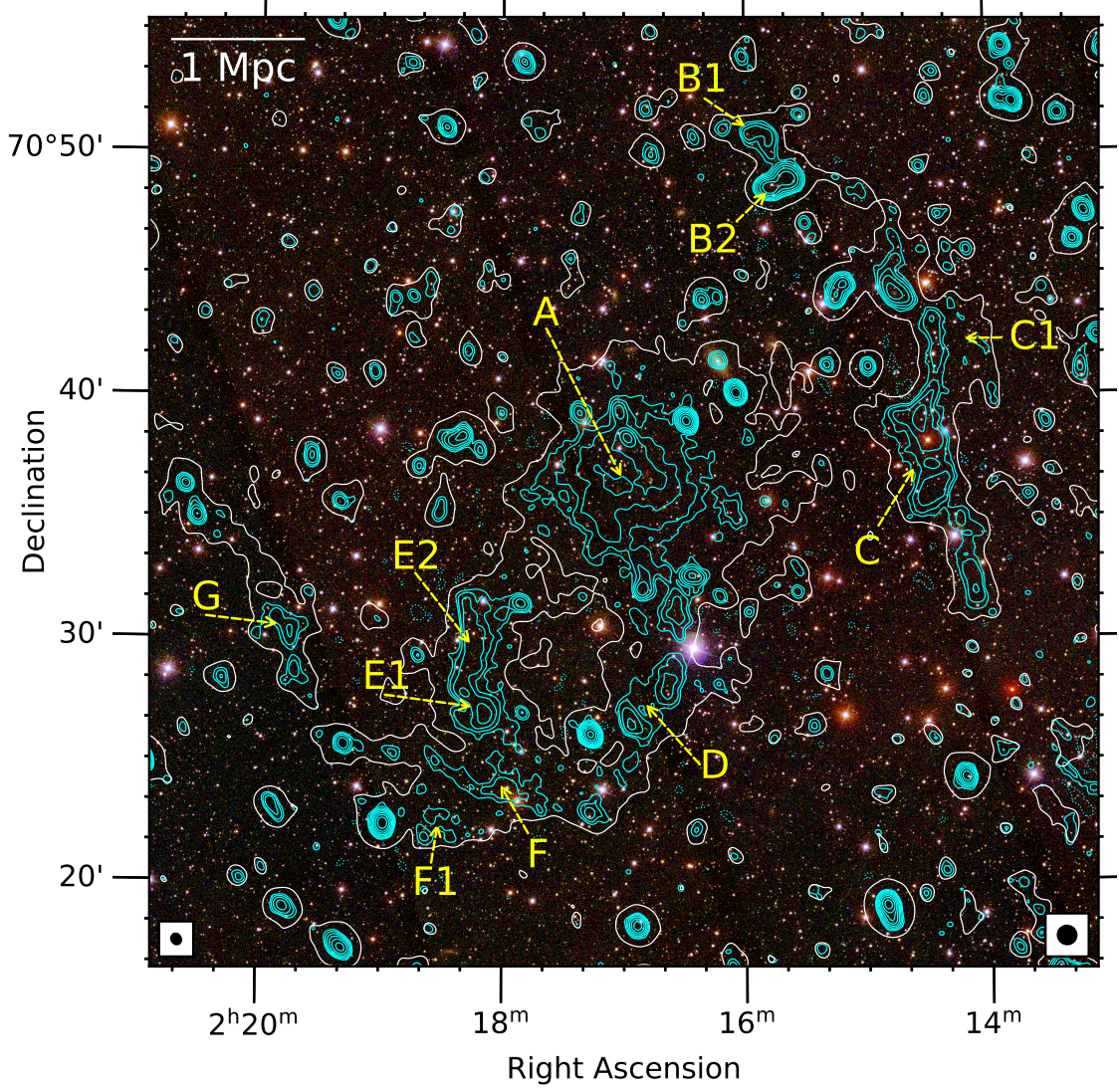


Fig. 2: SDSS colour image towards the ClG0217 field overlaid with LOFAR 141 MHz ($26.6'' \times 22.5''$)-resolution cyan contours. The contour levels are $\pm[1, 3, 9, 27, 81] \times 3\sigma$, where $\sigma = 240 \mu\text{Jy beam}^{-1}$. The white 2σ , where $\sigma = 335 \mu\text{Jy beam}^{-1}$, LOFAR contour has a lower resolution of $45.7'' \times 44.7''$. Compact sources are not subtracted from the images. The synthesised beams are shown at the bottom left/right corners. The labelling of the sources are adapted from Brown et al. (2011).

i.e. 800 kpc, which is likely due to the fact that the VLA C-array observations lack short baselines for the detection of large-scale emission from the halo (i.e. up to $10'$). In the southern and eastern regions the halo is connected to elongated diffuse sources D and E (Fig. 4). The connection between the halo and sources D and E can only be seen in the LOFAR image at 141 MHz, implying steep-spectrum nature of the diffuse radio emission in the regions between the sources. Multiple discrete sources are also embedded in the southern and northern regions of the halo.

The 141 MHz flux density of the radio halo measured within the 3σ contour is 597.7 ± 59.9 mJy. This increases by 2.6 percent to 613.4 ± 61.5 mJy when all pixels above 2σ are included. At 1.4 GHz, we measure the flux density for the halo integrating over the 3σ and 2σ regions to be 46.9 ± 2.5 mJy and 51.1 ± 2.7 mJy (a 9.0 percent increase), respectively. Using the same VLA data sets, Brown et al. (2011) reported a higher value (i.e. 58.6 ± 0.9 mJy or ~ 15 percent higher than our 2σ measurement) for the halo flux density at 1.4 GHz. Our measurements are summarised in Tab. 3.

We note that the application of a threshold cut to the pixel values used when integrating the halo flux might bias the measurement low, due to missing flux from the faint emission in the outer regions of the radio halo. For comparison and better recovery of the low SB emission, we fit the SB of the halo with a 2D circular exponential model of the form

$$I(r) = I_0 \exp(-r/r_e), \quad (1)$$

where the fitting parameters I_0 and r_e are the SB at the halo centre and the e -folding radius. The radial SB of radio halos that have regularly round morphology is usually described by an exponential model (Murgia et al. 2009). We made use of the Halo-FDCA⁴ code (Boxelaar et al. 2021) that has been used to estimate the flux densities of the radio halos detected with the LoTSS survey in the HETDEX field (van Weeren et al. 2020). The code runs Markov Chain Monte-Carlo method to search for the best-fit parameters and the associated uncertainties. When the best-fit parameters are found, the flux density is integrated

⁴ <https://github.com/JortBox/Halo-FDCA>

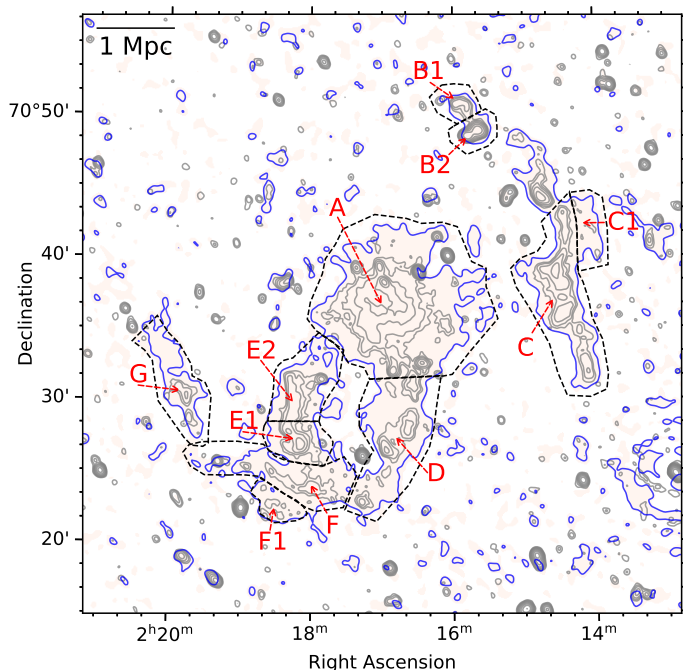


Fig. 3: The black dashed lines in this image show the regions used to measure the flux densities.

to a radius defined by users. In CIG0217, when calculating of the total errors, we add in quadrature the uncertainties associated with the model fitting and the LOFAR and VLA flux calibration (i.e. 10% and 5%, respectively). The flux density for the halo in CIG2017 is 623.6 ± 62.7 at 141 MHz and 58.3 ± 3.4 at 1.4 GHz which is consistent within 1σ and 2σ for the LOFAR and VLA data, respectively, with those estimated using the 2σ threshold cut method. The corresponding radio power is $56.9 \pm 5.7 \times 10^{24} \text{ W Hz}^{-1}$ at 141 MHz and is $53.2 \pm 3.1 \times 10^{23} \text{ W Hz}^{-1}$ at 1.4 GHz. The obtained radio power is consistent with the correlation between radio power and cluster mass (see Fig. 8). The best-fit parameters are $I_0 = 15.51 \pm 0.18 \mu\text{Jy arcsec}^{-2}$ and $r_e = 255 \pm 2 \text{ kpc}$ at 141 MHz and $I_0 = 1.19 \pm 0.04 \mu\text{Jy arcsec}^{-2}$ and $r_e = 281 \pm 7 \text{ kpc}$ at 1.4 GHz. The e -folding radius at 1.4 GHz is larger than that at 144 MHz, implying that the halo at high frequencies can be larger, but unable to be detected with the current shallow data. We note that the flux density above is integrated within a radius of $4r_e$ which is slightly larger than the radius of the halo within the 2σ contours (i.e. $r_e = 900 \text{ kpc}$). This consists of 90 percent of the flux density when integrating the flux density to infinity. The corner plots showing the constraints of the fitting are presented in Fig. C.1.

Using the flux density measurements obtained from the exponential model fitting, we find that the integrated spectral index between 141 MHz and 1.4 GHz for the radio halo is -1.02 ± 0.05 , which is consistent with the value of -1.07 ± 0.05 that is obtained using the measurements from the 2σ threshold cut method. However, our estimates are flatter than the 325 MHz – 1.4 GHz spectral index of -1.34 ± 0.19 reported in Brown et al. (2011) where they used the 325 MHz flux density of $326 \pm 30 \text{ mJy}$ for the halo. However, we note that the 325 MHz observations have low resolution that are unable to resolve the compact sources to the N edge of the halo (Fig. 6). These compact sources likely contaminate the flux measurement at 325 MHz, making the halo spectrum steeper than its true value.

In Fig. 7 we present the low ($46''$) resolution spectral index map of CIG0217. The cutout images show the distribution of the spectral index in the source regions at the resolution of $16''$. In the central region of the halo, the spectral index remains roughly constant, but it seems to flatten in the outer regions where the spectral index might be contaminated by the imperfection of the subtraction of discrete sources. In Fig. 11 we examine the radial spectral index profile where the contaminating sources are masked out. The spectral indices are extracted from the annuli that have a size of $60''$. The spectral index profile suggests a uniform spectral index of -1.07 ± 0.02 within a radius of 640 kpc (i.e. over an area of 1.3 Mpc^2). In the outer region ($r = 820 \text{ kpc}$), the index becomes steeper than -1.15 ± 0.03 . We note that the errors estimated in the profile do not include the uncertainty associated with the flux scale calibration as, if included, the spectral index is systematically, rather than randomly impacted. However, if the flux scale uncertainty is added in quadrature with the image noise, the typical errors for the spectral indices are 0.06 that does not change our conclusion on the spectral index uniformity in the central region of the radio halo.

3.1.2. The NE edge

A recent study by Zhang et al. (2020) found discontinuities in the X-ray SB towards the N and S edges of the radio halo in the VLA 1.4 GHz data. In addition to the two reported edges, we note that the NE edge of the radio halo in the LOFAR 141 MHz map (Fig. 4) could be associated with a new X-ray SB discontinuity. We extract an X-ray SB profile using the box region defined in Fig. 9 and fit it using a projected broken power law density model (Owers et al. 2009). We obtain a best-fit density jump of 1.92 ± 0.34 at the radius of $195'' \pm 8''$. Meanwhile, we extract the radio SB profile in this region from the $46''$ resolution map. The radio SB follows the trend of the X-ray SB before the jump and drops quickly at the X-ray SB jump. The six outermost radio data points below $1.5\sigma_{\text{rms}}$ are regarded as the radio background. The new NE X-ray edge partly overlaps with the previously reported N edge.

Although the nature of the X-ray SB discontinuities is unknown and the relation between the N and the NE discontinuities is unclear yet, if they have a nature of a shock front, they might affect the spectra of the non-thermal emission in the regions. We examine the spectral index trend towards the N and S regions of the halo using the $46''$ -resolution spectral index image. The spectral indices are extracted from the N and S sectors (see Fig. 11). The width of the radial sub-regions is taken to be the size of the synthesised beam (i.e. $46''$ or 140 kpc). The profiles in Fig. 11 show that the spectral index does not change (i.e. within 1σ) towards the directions of the X-ray SB jumps. This might be because the spectral index map with the resolution of $46''$ (140 kpc) cannot resolve the spatial spectral structure of the diffuse radio emission in this region of the halo. Although there are hints of the spectral flattening towards the regions of the X-ray SB jumps, high uncertainties in the spectral index measurements prevent us from drawing a conclusion on the trend. Future deep, high-resolution radio observations will be necessary.

3.1.3. Thermal and non-thermal correlation

With the current data, the X-ray thermal emission from the ICM of CIG0217 is approximately as extended as the size of the radio emission (Fig. 4). It is noted that the *Chandra* data was obtained from the shallow 25 ks observations that might not detect the

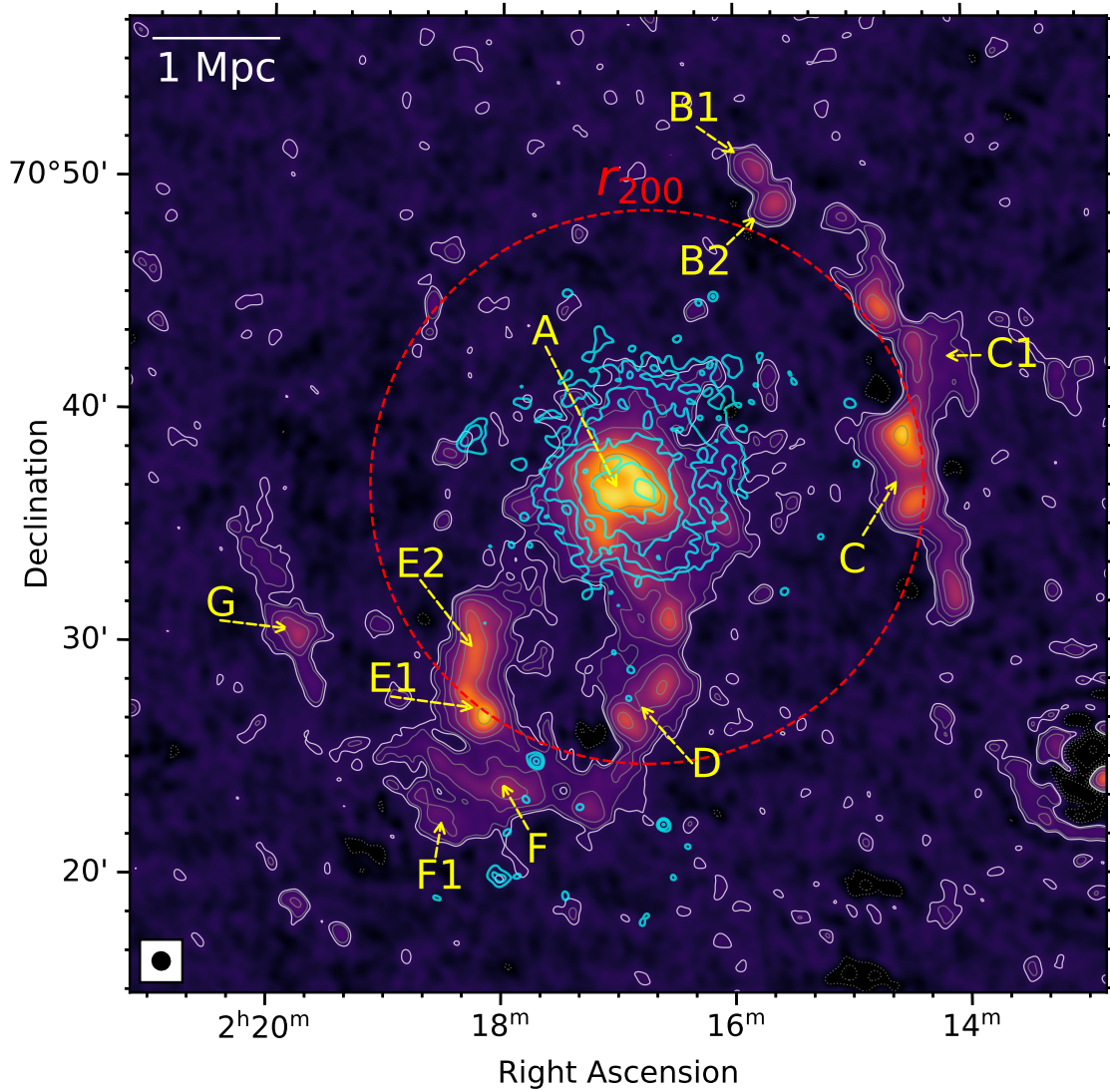


Fig. 4: LOFAR ($45.7'' \times 44.7''$)-resolution image of ClG0217 (see Tab. 2 for the image properties). The contaminating discrete sources are removed from the data (Sec. 2.3). The LOFAR gray and *Chandra* cyan contours are drawn at $\pm[1, 2, 4, 8, 16] \times 3\sigma$, where $\sigma = 240 \mu\text{Jy beam}^{-1}$ and $\sigma_{\text{Chandra}} = 1.3 \times 10^{-6} \text{cts arcmin}^{-2} \text{cm}^{-2}$. The LOFAR white contour is drawn at 2σ . The *Chandra* data is smoothed with a Gaussian beam of 5-pixel sigma where pixel size is $1.968''$. The red dashed circle shows the $r_{200} = 2.3 \text{ Mpc}$ (Zhang et al. 2020).

faint emission in the outer region of the cluster. The intensity of the X-ray and radio diffuse emission in the halo region is spatially correlated. This is clearest in the central region of the halo where elongated sub-structures in the X-ray and radio emission are seen in the NE-SW direction.

The correlation between thermal and non-thermal emission in the cluster central region has been found to follow a power-law relation,

$$\log_{10} I_R = a + b \times \log_{10} I_X, \quad (2)$$

where a and b are free parameters (e.g. Govoni et al. 2001a; Feretti et al. 2001; Govoni et al. 2001b; Bruno et al. 2021; Rajpurohit et al. 2021). The parameter b describes how the X-ray and radio SB is correlated. For $b = 1$, the SB of the thermal and non-thermal emission is linearly related over the source. Whereas, the SB values are sub-linearly and super-linearly related in cases of $b < 1$ and $b > 1$, respectively. In case of sub-/super-linear correlation, the non-thermal components radially decline slower/faster than the thermal ones. We quantita-

tively examine the correlation between the thermal X-ray and non-thermal radio emission from the halo of ClG0217 by performing a point-to-point analysis with the *Chandra* and LOFAR 141 MHz/VLA 1.4 GHz data. We extract the SB of the X-ray and radio emission from 48 square regions that have sizes of $60'' \times 60''$ (i.e. $182 \times 182 \text{ kpc}^2$), covering up to 1.5 Mpc^2 area of the halo (Fig. 12). The size of the square regions is set to be larger than the size of the synthesised beam which is $46''$. The regions are selected within the LOFAR 2σ contours, excluding the flat spectral index regions that are likely to be affected by the imperfect subtraction of compact sources. The *Chandra* image is smoothed with a 2D Gaussian function that has a kernel of 5 pixels (i.e. $5 \times 1.968''$). We perform a Bayesian linear regression using the `linmix` package⁵ that takes into account the uncertainties of both X-ray and radio data (Kelly 2007). The scatter plot in Fig. 12 (middle) indicates linear and sub-linear positive correlations with $b_{141 \text{ MHz}} = 1.03 \pm 0.09$ and $b_{1.4 \text{ GHz}} = 0.81 \pm 0.06$,

⁵ <https://github.com/jmeyers314/linmix>

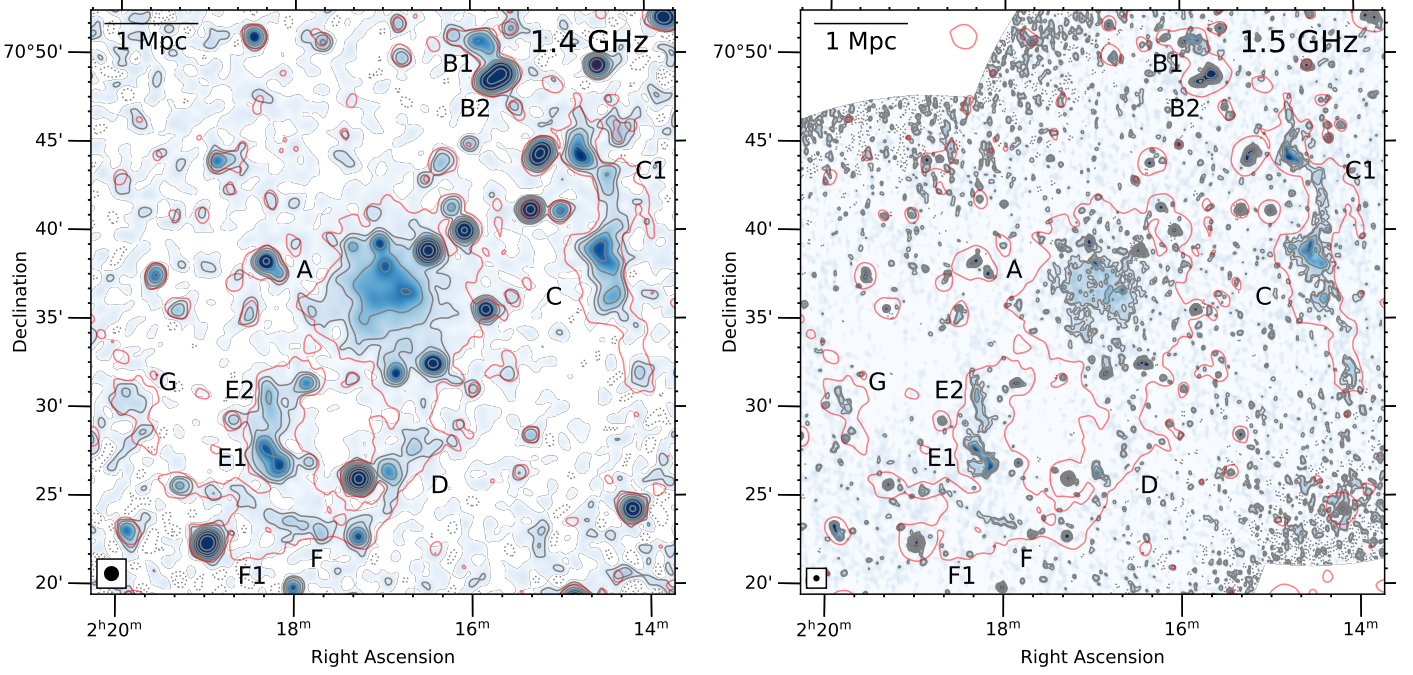


Fig. 5: VLA 1.4 GHz (*left*) and 1.5 GHz (*right*) images of CIG0217. The first (gray) contour starts from 3σ , where $\sigma_{1.4 \text{ GHz}} = 85 \mu\text{Jy beam}^{-1}$ and $\sigma_{1.5 \text{ GHz}} = 40 \mu\text{Jy beam}^{-1}$. The subsequent contours are multiplied by a factor of 2. The synthesized beams are drawn in the bottom left corners (i.e. $46'' \times 46''$ and $16'' \times 16''$ for the 1.4 GHz and 1.5 GHz images, respectively.) The LOFAR 3σ contour (i.e. same as that in Fig. 4) is shown in red.

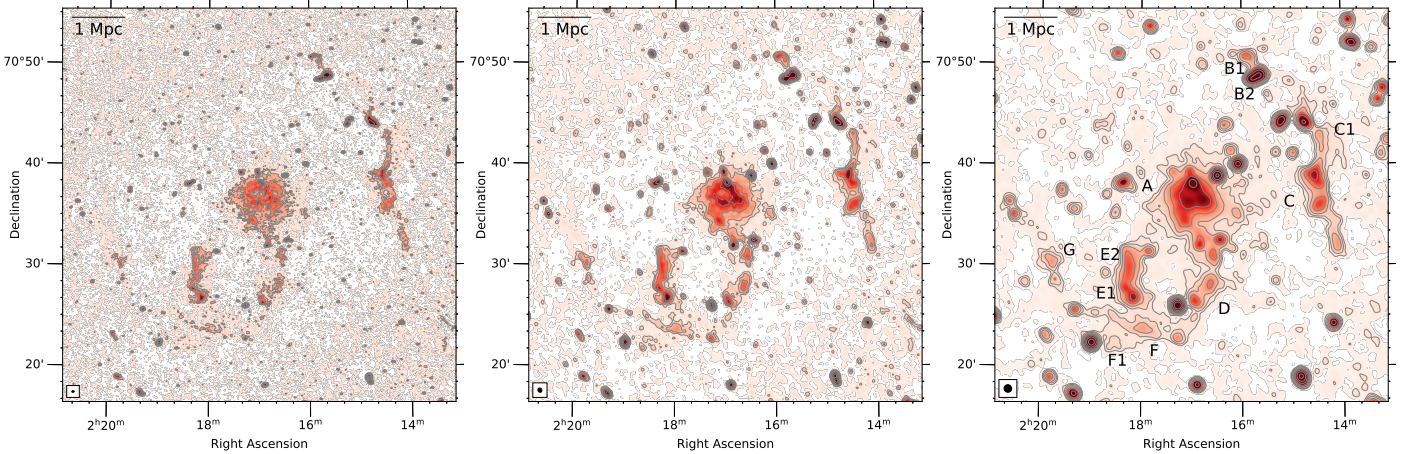


Fig. 6: LOFAR 141 MHz images of CIG0217 at high, medium, and low resolutions. The resolution of the images (from left to right) are $14.6'' \times 10.1''$, $26.6'' \times 22.5''$, and $45.7'' \times 44.7''$. The first contour is shown at 3σ , where $\sigma_{\text{rms}} = 160, 240, \text{ and } 330 \mu\text{Jy beam}^{-1}$, respectively. The next contours are multiplied by a factor of 2.

respectively. We also report the Pearson's (linear) correlation coefficients, including degree of freedom (DoF) and the p -value in Tab. 4. The results suggest tight correlations between the radio and X-ray emission from the halo. The obtained coefficients b imply that the non-thermal components at 1.4 GHz declines more slowly than that at 141 MHz which is in line with the tentative flattened trend in our spectral index radial profile within a radius of 640 kpc in Fig. 11.

In a similar manner, we extracted the spectral indices in the square regions to study its relation with the X-ray SB that is fit with a relation of the form,

$$\alpha = a + b \times \log_{10} I_X. \quad (3)$$

The scatter plot between the spectral indices and X-ray SB is shown in Fig. 12 (*right*). The obtained regression slope of $b = -0.01 \pm 0.05$ suggests that the spectral index in the halo regions is independent from the X-ray SB change. This is consistent with the Pearson's correlation coefficient of $r = -0.21$ in Tab. 4. As the square regions where the spectral indices are calculated are within a radius of 640 kpc, this result is in line with the spectral index profile shown in Fig. 11. We estimate the mean spectral index over the square regions to be -1.03 ± 0.13 , consistent with the integrated spectral index for the halo in Sec. 3.1.

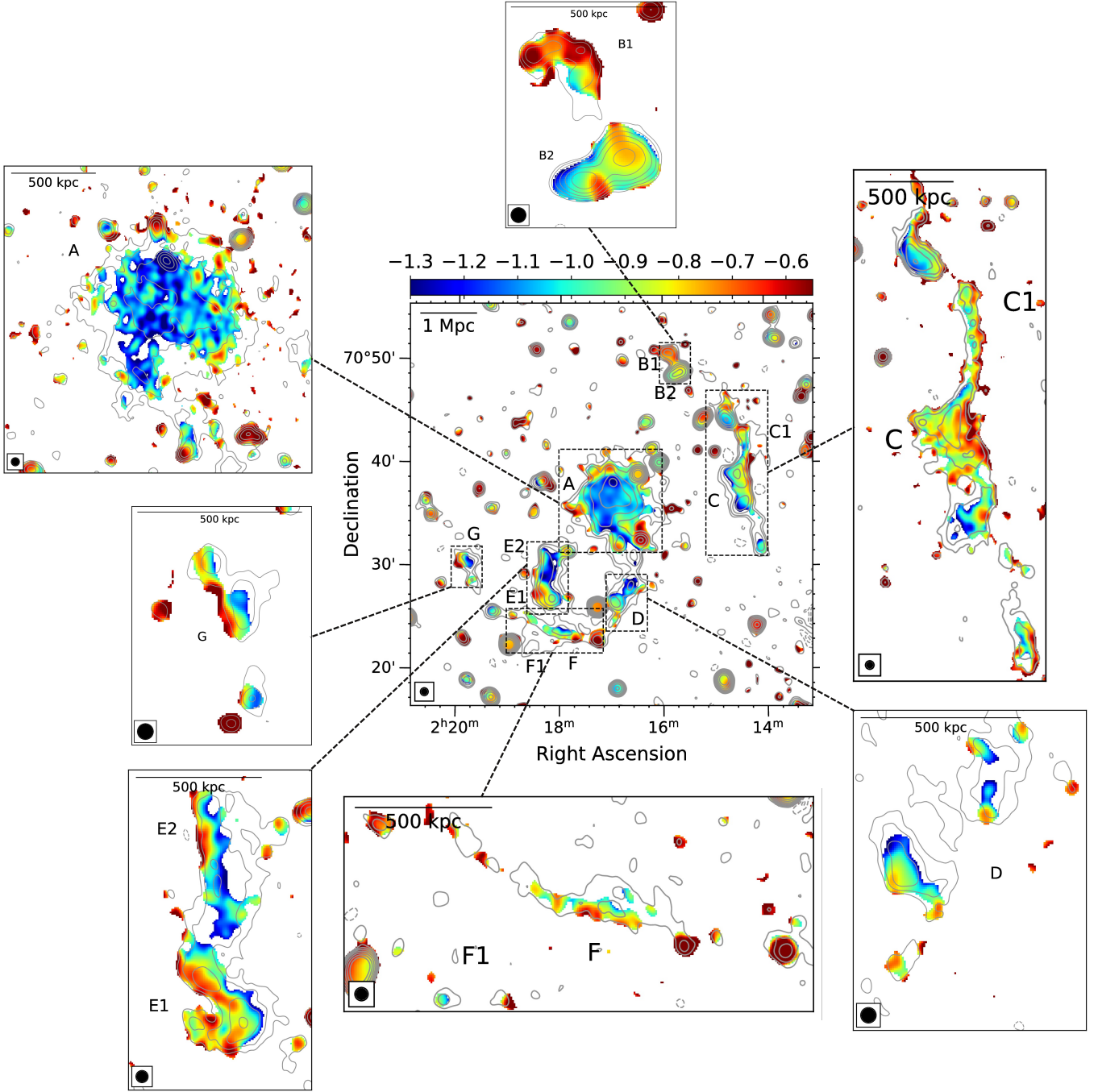


Fig. 7: Spectral index map (central) between 141 MHz and 1.4 GHz at the resolution of $46''$. The cutout images show the distribution of spectral indices between 141 MHz and 1.5 GHz at $16''$ resolution. The LOFAR contour levels are $\pm[1, 2, 4, 8, 16] \times 3\sigma$, where $\sigma = 345 \mu\text{Jy beam}^{-1}$ ($\text{beam}_{\text{FWHM}} = 46''$) and $\sigma = 190 \mu\text{Jy beam}^{-1}$ ($\text{beam}_{\text{FWHM}} = 16''$) for the central and the cutout images, respectively. The corresponding maps for the spectral index errors are shown in Fig. A.1.

3.2. Peripheral diffuse sources

Source C is located $15'$ to the west from the cluster centre and was classified as a radio relic by Brown et al. (2011). The projected length at 1.4 GHz is 1.7 Mpc (Fig. 5). With the deep, low-frequency observations of LOFAR, the relic is 35% longer in the LOFAR images (i.e. 2.3 Mpc). In these measurements, we do not include the bright, compact source to the north of the relic (see Fig. 3). An SDSS optical counterpart in the radio emission peak suggests that the radio emission is originated from a radio galaxy

(Fig. 2). The width of the relic C in projection is 620 kpc in the middle region, and it gets narrower towards the south and north (280 kpc). In the NW region of the relic, a diffuse, faint source, namely C1, is detected with LOFAR (Figs. 2 and 4), but it is not seen in the VLA images (Fig. 5). We estimate that the 141 MHz–1.4 GHz spectral index of C1 is steeper than -1.7 . For the relic C, we measure a flux density at 141 MHz and 1.4 GHz within the LOFAR 2σ region and summarise these measurements in Tab. 3. The integrated spectral index of the relic C is -1.01 ± 0.05 that is within typical range for known radio relics (e.g. van Weeren

Table 3: Radio source properties

Source	$S_{141\text{ MHz}}^a$ [mJy]	$P_{141\text{ MHz}}^b$ [10^{24} W Hz^{-1}]	$S_{1.4\text{ GHz}}^a$ [mJy]	$P_{1.4\text{ GHz}}^b$ [10^{23} W Hz^{-1}]	α	LAS ^c [Mpc]
A	613.4 ± 61.5 623.6 ± 62.7^d	56.4 ± 5.7 56.9 ± 5.7^d	51.1 ± 2.7 58.3 ± 3.4^d	47.0 ± 2.5 53.2 ± 3.1^d	-1.07 ± 0.05 -1.02 ± 0.05^d	1.8 –
B1	12.6 ± 1.5	1.1 ± 0.1	4.5 ± 0.3	3.7 ± 0.3	-0.45 ± 0.06	0.3
B2	16.6 ± 1.8	1.4 ± 0.2	4.6 ± 0.3	3.9 ± 0.3	-0.55 ± 0.05	–
C	211.4 ± 21.3	19.3 ± 2.0	20.3 ± 1.1	18.5 ± 1.0	-1.01 ± 0.05	2.3
C1	13.7 ± 1.8	1.3 ± 0.2	$< 0.3^c$	< 0.3	< -1.7	0.7
D	127.0 ± 13.0	12.3 ± 1.3	5.7 ± 0.5	5.5 ± 0.5	-1.34 ± 0.06	1.8
E1	84.2 ± 8.5	7.6 ± 0.8	9.7 ± 0.6	8.7 ± 0.5	-0.93 ± 0.05	0.5
E2	93.3 ± 9.5	8.8 ± 0.9	5.9 ± 0.4	5.5 ± 0.4	-1.19 ± 0.05	1.0
F	59.8 ± 6.3	5.5 ± 0.6	4.8 ± 0.4	4.4 ± 0.4	-1.09 ± 0.06	1.7
F1	15.1 ± 1.8	1.6 ± 0.2	$< 0.3^c$	< 0.3	< -1.7	0.6
G	31.4 ± 3.5	2.9 ± 0.3	3.1 ± 0.3	2.8 ± 0.3	-1.00 ± 0.06	1.6

Notes: The regions where the flux densities are extracted are shown in Fig. 3. ^a: the flux density is calculated for all pixels that are detected above 2σ , except in the case of ^d where flux density is obtained by fitting the surface brightness of the halo with a 2D circular model. ^b: k-corrected radio power, $P = 4\pi D_L^2 S_\nu / (1+z)^{(1+\alpha)}$, where D_L is the luminosity distance. ^c: Largest Angular Size.

^c: upper limit estimated by $\sigma \propto \sqrt{N}$, where N is the source area in beam unit.

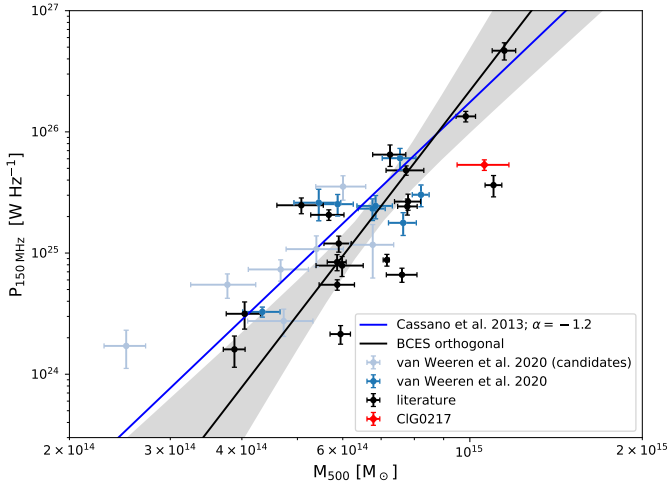


Fig. 8: The $P_{150\text{ MHz}} - M_{500}$ correlation including the data point for the radio halo in CIG0217 (in red). The plot is adapted from van Weeren et al. (2020).

Table 4: Parameters for the radio and X-ray SB correlation.

	b	r	DoF	p
LOFAR	1.03 ± 0.09	0.91	43	< 0.001
VLA	0.81 ± 0.06	0.97	34	< 0.001
α	-0.01 ± 0.05	-0.21	34	0.23

et al. 2019) and is significantly different from that of C1, implying their different origins. A spectral steepening across the width of the relic towards the cluster centre is seen in the spectral index map in Figs. 7 (see the cutout image for source C) and 10. In the middle region, the spectral index decreases from -0.72 on the western side to -1.35 . This result provides important evidence for the classification of the source as a radio relic.

Source D, F, and G in Figs. 2 and 4 are more extended at 141 MHz compared to 1.4 GHz (see Tab. 3 for the measurements of their extension). Due to its elongated shape and location, source D was thought to be an internal filament (Brown et al. 2011). In the LOFAR images, the source extends further

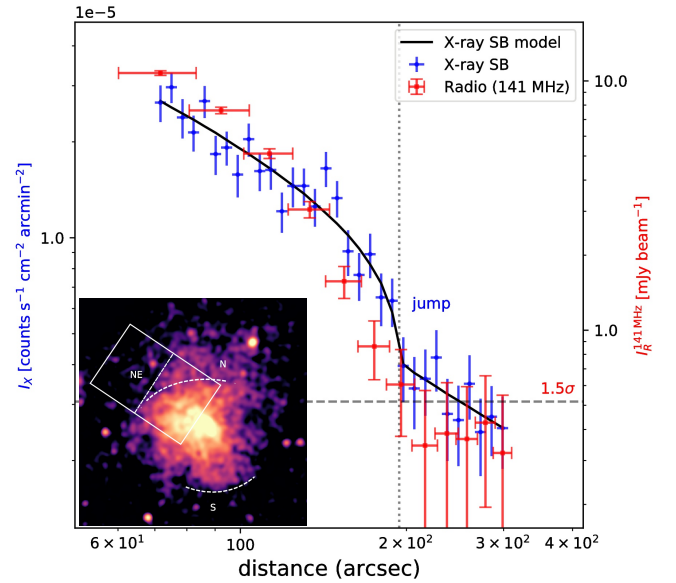


Fig. 9: X-ray and radio (141 MHz) SB profiles towards the NE direction of the halo. The X-ray SB model indicates a discontinuity marked by the vertical dotted line. In the overlay *Chandra* image, the extracted NE region is shown with the rectangles. The dashed N and S arcs are the SB edges found by Zhang et al. (2020).

than previously known in the NW–SE direction and its NW region is connected with the radio halo (source A) whilst its SE region is connected with source F. The extension of source D along its width (i.e. 600 kpc in the NE–SW direction; Fig. 2) suggests that it does not consist of discrete sources. The sources F and G were identified as radio relics by Brown et al. (2011) and are oriented in the EW and NS directions, respectively. The clear connection between D and F suggests that they belong to a single structure with a projected size of 3.5 Mpc. This increase to 5.1 Mpc if source G is included. On the outer region of source F towards the SE, an excess of diffuse emission, namely F1, is only detected at 141 MHz which suggests its steep spectral index. We find that the spectral index of F1 is steeper than -1.7 .

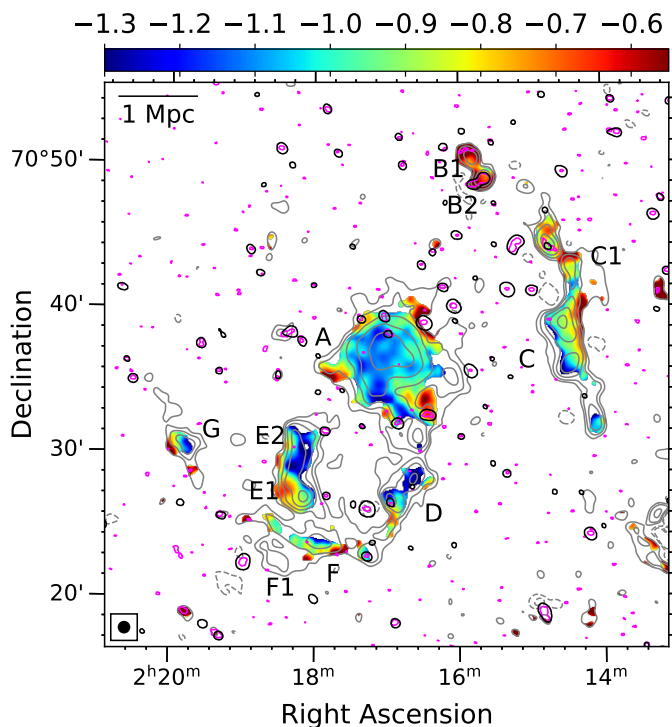


Fig. 10: Spectral index map at $46''$ resolution. The contaminating discrete sources are removed from the data and are marked with the magenta and black contours for the LOFAR and VLA detected sources, respectively. The LOFAR gray contour are drawn at $\pm[1, 2, 4, 8, 16] \times 3\sigma$, where $\sigma = 345 \mu\text{Jy beam}^{-1}$ ($\text{beam}_{\text{FWHM}} = 46''$). The spectral index error map is shown in Fig. A.1.

The flux densities and spectral indices for these sources are reported in Tab. 3. The spectral index distribution maps in Figs. 7 and 10 show the spectral steepening across the sources D, F, and G. Based on the spectral and morphological properties of source D, we suggest that it is a radio relic. Our results on the spectral steepening of F and G also support the relic classification of these sources by Brown et al. (2011).

Source E was identified as an internal filament with the VLA 1.4 GHz observations by Brown et al. (2011). With the LOFAR 141 MHz and VLA 1.5 GHz high-resolution data in Figs. 6 and 5 (right), the source is resolved showing two parts. The southern part has a morphology typical of a double-lobe radio galaxy that has a SDSS optical counterpart (namely, J021814.33+702724.0 at R.A.= $02^{\text{h}}18^{\text{m}}14.33^{\text{s}}$, Dec.= $+70^{\circ}27'24.07''$) reported in the SDSS catalogue (Alam et al. 2015). The optical source is better seen in the Pan-STARRS image in Fig. B.1 (with object identification: 192540345597208886; Chambers et al. 2019). No redshift data is reported for this optical source in the SDSS and Pan-STARRS catalogues. The morphology of the lobes suggests that it is a typical FR-I galaxy. The southern lobe of the AGN is bent towards the eastern direction. The northern part of E has an elongated shape that connects with a lobe of the southern radio galaxy. We interpret source E being a radio galaxy that is moving in the NW-SE direction and leaving the tail of radio emission behind.

Source B was suggested to be a radio relic by Brown et al. (2011), but in our high-resolution images (Figs. 6 and 5, right) it is composed of a bent-tail radio galaxy to the north and a radio galaxy with two lobes to the south. These radio

galaxies are also detected with the SDSS and Pan-STARRS optical surveys (see Figs. 2 and B.1). The SDSS identification is J021558.09+705040.1 ($z = 0.1962 \pm 0.0802$) and J021542.94+704832.3 for the north and south sources, respectively.

4. Discussions

4.1. Radio halo

The presence of the radio halo in ClG0217 is confirmed with the LOFAR 141 MHz and VLA 1.5 GHz observations. The projected diameter of the halo at 141 MHz is 1.8 Mpc which is more extended than previously detected at 1.4 GHz (Brown et al. 2011). The integrated spectral index for the halo is -1.02 ± 0.05 which is flatter than that estimated in Brown et al. (2011). We discuss the spectral index properties and the correlation between thermal and non-thermal components below.

4.1.1. Spectral index variations

Spatial distribution of the spectral index in halos provides insight into the physical mechanisms responsible for the particle acceleration and magnetic field amplification in radio halos. In general, spatial distribution of spectral index provides information on turbulent scales, transport of particles and magnetic field in the ICM. For example, homogeneous models where turbulence and magnetic field strength are uniform in the emitting volume predict a uniform distribution of the spectral index. On the other hand, models with inhomogeneous conditions of turbulence and magnetic field predict variations in the spectral indices in the entire emitting volume, depending on how fast transport of particles, diffusion of magnetic field, and turbulent scales are.

Observations have shown complex pictures of the radial distribution of the spectral index in radio halos. Three cases where the average radial spectral index steepens in the peripheral regions have been found (i.e. Abell 2744; Pearce et al. 2017, MACS J0717.5+3745 Rajpurohit et al. 2021). In some other cases no firm detection of radial spectral steepening feature is detected (e.g. Coma C⁶; Giovannini et al. 1993, Abell 665⁶, Abell 2163⁶; Feretti et al. 2004, Abell 2219; Orrù et al. 2007). In some ongoing merging clusters, a uniform distribution of the spectral index over a large fraction of the halos was also detected (e.g. the Toothbrush cluster; van Weeren et al. 2016a; Rajpurohit et al. 2018; de Gasperin et al. 2020; Rajpurohit et al. 2020, the Sausage cluster; Hoang et al. 2017; Gennaro et al. 2018, and Abell 520; Hoang et al. 2019a).

In ClG0217, a spectral steepening is detected beyond 820 kpc from the cluster centre (Fig. 11, right). However, within 640 kpc, the radial profile is roughly constant although there is a hint of spectral flattening. We note that X-ray SB discontinuities are detected at the edges of the northern and southern regions (within 640 kpc) (Zhang et al. 2020). Although the nature of the X-ray discontinuities (i.e. shock or cold front) is still unknown, they might affect the observed radio spectrum of the halo through the (re-)acceleration of the CRs and/or amplification of magnetic field. In some clusters, shock fronts are observed at the edges of radio halos, including Abell 520 (Markevitch et al. 2005), the Bullet cluster (Shimwell et al. 2014), the Coma cluster (i.e. the western edges of the halo Brown & Rudnick 2011),

⁶ The uncertainty of the spectral measurement in these cases is high due to the mismatching of the uv -coverages in the observations, as pointed out by Botteon et al. 2020b.

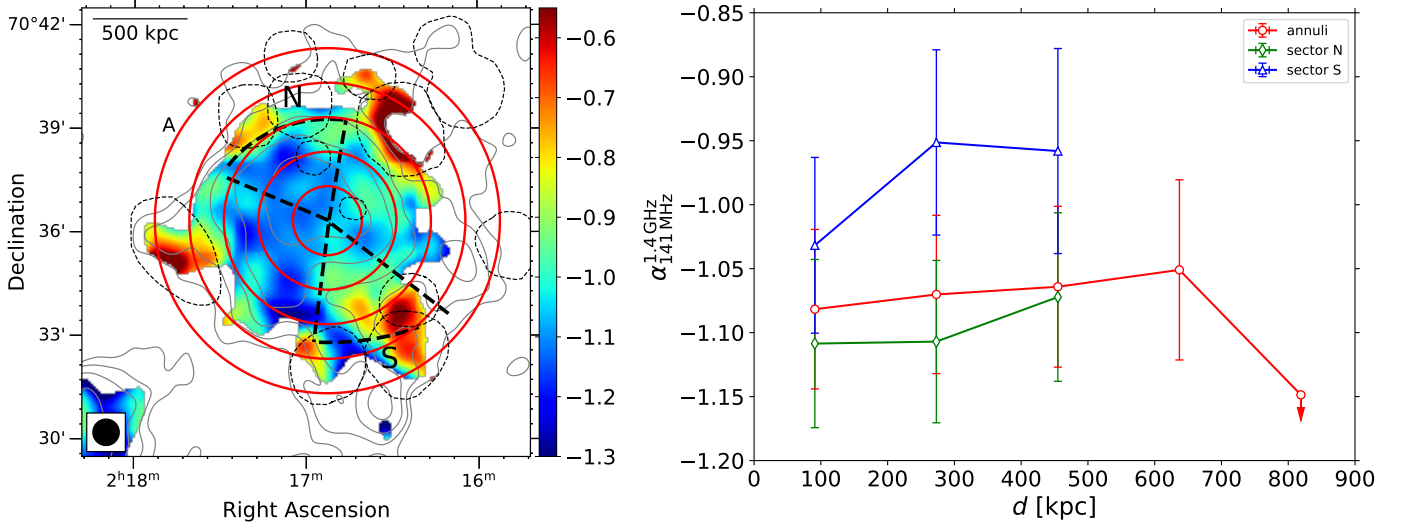


Fig. 11: *Left*: 141 MHz – 1.4 GHz spectral index map in the halo region. The red annuli and black dashed sectors are where the spectral indices are extracted. The outermost regions of the N and S sectors are where X-ray SB discontinuities are found in Zhang et al. (2020). The thin dashed lines are the regions where discrete sources are subtracted or show locally flat spectra. *Right*: The spectral index profiles from the halo centre towards the outskirts and towards the N and S sectors are plotted.

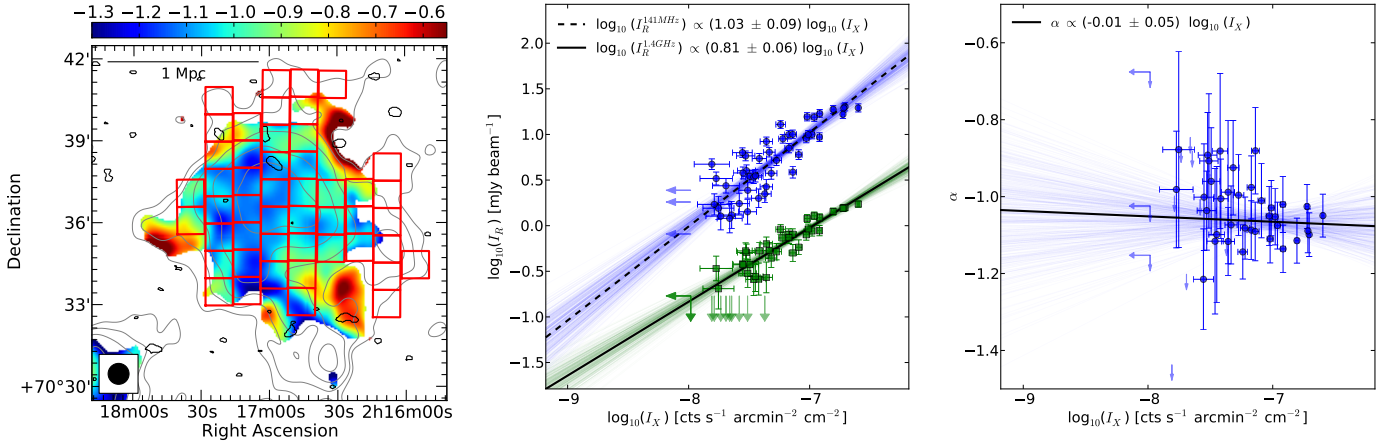


Fig. 12: *Left*: Regions where radio and X-ray data are extracted. *Middle*: Correlation between radio and X-ray SB. *Right*: Scatter plot of the radio spectral index and X-ray SB. In both plots, the 2σ upper limits are shown with the downward/leftward arrows.

and the Toothbrush (i.e. the S edge van Weeren et al. 2016a). Among these cases spectral flattening at the edges has been seen in two clusters, including the SW region of Abell 520 (Hoang et al. 2019a) and the southern shock of the Toothbrush (Rajpurohit et al. 2018). The halo in CIG0217 might be the third case if future deep radio observations confirm the radial spectral trend.

4.1.2. Thermal and non-thermal correlation

The radio and X-ray emission in the halo of CIG0217 are found to be spatially correlated (Sec. 3.1.3). In particular, the radio and X-ray sub-structures in the central region of the halo are found to have similar shape and orientation (Fig. 4). Quantitatively, the radio and X-ray SB is consistent with the linear relation at 141 MHz (i.e. $\log_{10} I_R \propto b \times \log_{10} I_X$ where $b_{141\text{ MHz}} = 1.03 \pm 0.09$), and they follow a sub-linear relation at 1.4 GHz (i.e. with $b_{1.4\text{ GHz}} = 0.81 \pm 0.06$). The spatial correlation suggests a tight connection between the thermal gas and non-thermal components (i.e. relativistic electrons and magnetic field) in the ICM.

Our results are similar to some cases where the radio and X-ray relation is linear/sub-linear (i.e. $b \sim 0.64 - 1$) regardless of the morphology of the radio halos (e.g. Feretti et al. 2001; Govoni et al. 2001a,b; Bruno et al. 2021; Rajpurohit et al. 2021; Botteon et al. 2020b). Also, a lower value of b at higher frequency suggests additional non-thermal processes in the outer regions of the halo where X-ray emission is fainter. In the halo of CIG0217, the lower coefficient b at high frequency likely associates with the presence of the X-ray SB discontinuities at the edges of the halo. The hint of this trend is also seen in A520 which hosts two X-ray SB jumps (i.e. a strong bow shock and a tentative shock/cool front) at the halo edges (Hoang et al. 2019b). They found $b_{145\text{ MHz}} = 0.34 \pm 0.11$, $b_{323\text{ MHz}} = 0.27 \pm 0.10$, and $b_{1.5\text{ GHz}} = 0.25 \pm 0.09$. However, an opposite trend (i.e. $b_{144\text{ MHz}} = 0.67 \pm 0.05$, $b_{1.5\text{ GHz}} = 0.81 \pm 0.09$, and $b_{3\text{ GHz}} = 0.98 \pm 0.09$) is observed in the halo of MACS J0717.5+3745 (Rajpurohit et al. 2021). The difference is likely due to the difference in the physical conditions in the two halos.

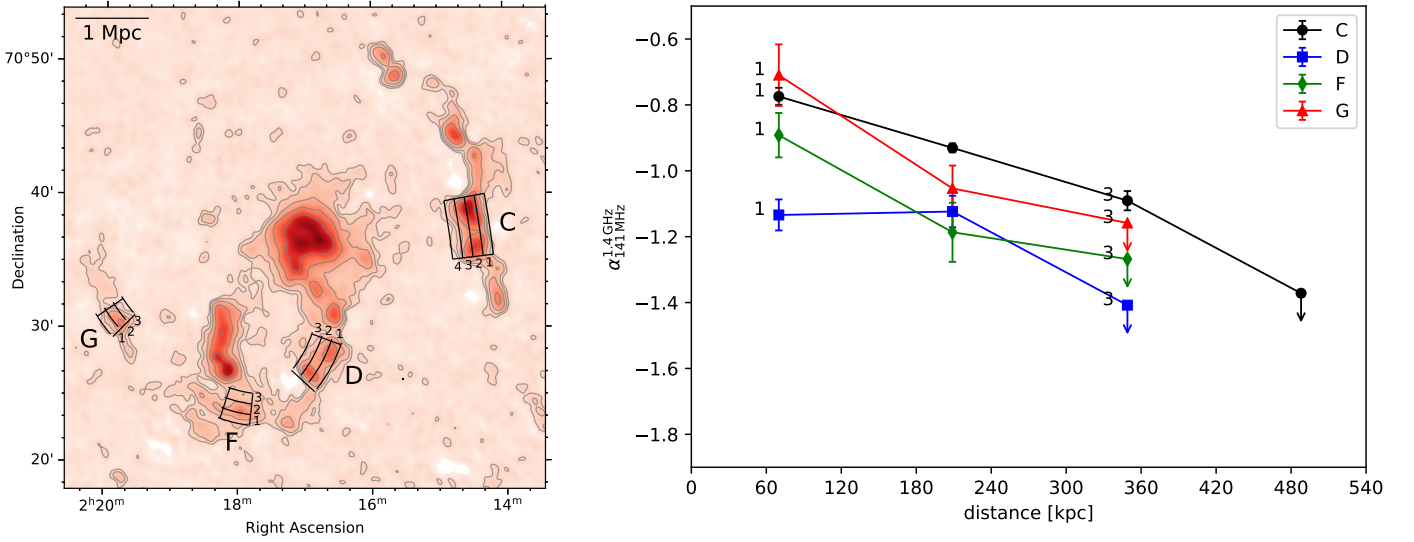


Fig. 13: *Left*: Regions where spectral indices are extracted. *Right*: Spectral index profiles across the width of the relics on the left panel. The downward arrows indicate the upper limit of the spectral indices. The error bars show the 1 σ uncertainties that are estimated from the image noise. The upper limits for the spectral indices (i.e. the arrows) are calculated using the upper limits of 2 σ for the 1.4 GHz emission.

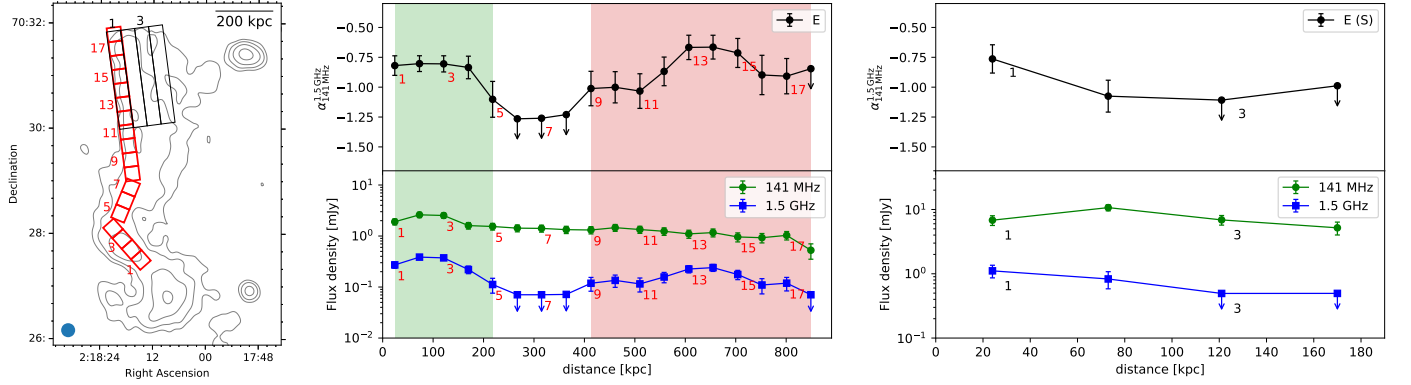


Fig. 14: *Left*: Regions over source E where SB and spectral indices are extracted and are shown in the *middle* and *right* panels. *Middle*: the SB and spectral index profiles along the SN direction (i.e. red boxes). *Right*: Similar to those in the *middle* panel, the profiles are calculated in the EW direction (i.e. black rectangles).

In homogeneous turbulence re-acceleration context, a broad spatial distribution of mildly relativistic seed electrons and of the turbulence are assumed to be uniform over a Mpc³ volume. The synchrotron power is,

$$P \propto \rho \frac{dV^3}{L} \frac{B^2}{B^2 + B_{\text{CMB}}^2}, \quad (4)$$

where ρ is the thermal particle density, dV is the turbulent velocity, and L is the corresponding turbulent scale. In the dynamo conditions, $B^2 \propto \rho dV^2$, the synchrotron power becomes,

$$P \propto \rho^2 \frac{1}{1 + (B/B_{\text{CMB}})^2}, \quad (5)$$

For weak magnetic field $B \ll B_{\text{CMB}}$ environments, where $B_{\text{CMB}} = 3.2(1+z)^2 \mu\text{G}$, the synchrotron power is linearly proportional to the square of thermal particle density ρ , i.e. $P \propto \rho^2$. At the ClG0217 redshift, the magnetic field strength is required to be much smaller than 4.5 μG . Our result on the linear slope of the thermal vs. non-thermal correlation at 141 MHz

($b_{141 \text{ MHz}} = 1.03 \pm 0.09$) is in line with this weak magnetic field conditions. In strong magnetic field ($B \gtrsim B_{\text{CMB}}$) environments, the non-thermal and thermal emission follows a sub-linear correlation. At higher frequencies, radio emission is more sensitive to stronger field strength and more energetic population of relativistic electrons. Given the weak magnetic field conditions in ClG0217, the 1.4 GHz sub-linear coefficient of $b_{1.4 \text{ GHz}} = 0.81 \pm 0.06$ suggests additional non-thermal processes that (re-)accelerate relativistic electrons in the outer regions of the halo (i.e. low X-ray SB regions). Our result is consistent with the radial spectral index analysis in Sec. 3.1.1.

4.2. Radio relics

4.2.1. Shock Mach numbers

The elongated shape, location, and the lack of optical counterparts of C, D, F, and G suggest that they are radio relics. The spectral steepening across their width further supports the classification (see Fig. 13). In the context of direct shock acceler-

Table 5: Shock properties of radio relics.

Source	α_{inj}	\mathcal{M}_{inj}	α_{int}	\mathcal{M}_{int}
C	-0.72 ± 0.05	$3.2^{+0.4}_{-0.3}$	-1.01 ± 0.05	14
D	-1.14 ± 0.07	$2.0^{+0.1}_{-0.1}$	-1.34 ± 0.06	$2.6^{+0.2}_{-0.2}$
F	-0.93 ± 0.08	$2.4^{+0.2}_{-0.2}$	-1.09 ± 0.06	$4.8^{+3.4}_{-1.0}$
G	-0.97 ± 0.16	$2.3^{+0.4}_{-0.2}$	-1.00 ± 0.06	≥ 5.8

ation model, the relativistic electrons emitting the radio synchrotron emission in radio relics are accelerated directly from thermal pool at shock fronts. The energy distribution of these relativistic electrons follows the standard power-law function $dN(p)/dp \propto p^{-\delta_{\text{inj}}}$, where $dN(p)$ is the number of particles in the energy range between p and $p + dp$ and $\delta_{\text{inj}} = 1 - 2\alpha_{\text{inj}}$ is the energy index. The spectral index of the injected relativistic electrons, α_{inj} , non-linearly depends on the Mach number of the shocks (e.g. Blandford & Eichler 1987),

$$\mathcal{M} = \sqrt{\frac{2\alpha_{\text{inj}} - 3}{2\alpha_{\text{inj}} + 1}}, \quad (6)$$

where $\alpha_{\text{inj}} > -0.5$. After being injected from the shock fronts the relativistic electrons start to lose their energy in the downstream region due to the synchrotron and inverse-Compton radiation, resulting steeper integrated spectral index over the source volume (Ginzburg & Syrovatskii 1969),

$$\alpha_{\text{int}} = \alpha_{\text{inj}} - 0.5. \quad (7)$$

The Mach numbers can be estimated through the discontinuity of X-ray SB or temperature jumps that associate with the particle density across the shock fronts. However, the X-ray *Chandra* data we use in this study is too shallow or does not cover the regions of the radio relics. To estimate the strength of the shocks associated with the relics, we calculate their Mach numbers using the injected spectra that are measured in the injection regions and the volume of the sources. In both methods we use the LOFAR 141 MHz and VLA 1.4 GHz 46''-resolution images (see Tab. 2 for image properties). We measure the injection spectral indices in the outer regions of the relics C, D, F, and G that have flattest spectra where the relativistic electrons are injected. Taking into account the image resolution, we set the width of the regions to be the same as the beam size (i.e. 46''). The corresponding Mach numbers are estimated using Eq. 6 and given in Tab. 5. The Mach numbers for these relics range between 2.0 and 3.2 that are typically found for shocks in merging clusters of galaxies (e.g. Markevitch & Vikhlinin 2007). Alternatively, the Mach numbers can be calculated from the volume integrated spectral index via Eq. 6 and 7. We use the integrated spectral indices for the relics in Tab. 3. The resulting Mach numbers for D and F are $2.6^{+0.2}_{-0.2}$ and $4.8^{+3.4}_{-1.0}$, respectively. These estimates are higher than those that we estimated with the injection spectral indices (Tab. 5). Previous studies have also found this systematic offsets between the estimates that use spatially resolved maps and integrated spectra (e.g. Stroe et al. 2013; Hoang et al. 2017, 2018). However, the integrated spectral index method when used for the relics C and G results in unrealistic Mach numbers for merger shocks. For instance, the integrated spectral index for C is -1.01 ± 0.06 that corresponds to a shock Mach number of 14 which cannot be found in merging galaxy clusters as it requires very different particle acceleration efficiency than those in other relics D and F. For the relic G, the integrated spectral index of -1.00 ± 0.06 implies an injection spectral index of -0.50 ± 0.06

which cannot be used for Eq. 7 (i.e. square root of a real negative number). This implies that the relic G is a clear example where Eq. 7 is invalid. In other words, the cooling time of the radio emitting particles is shorter than crossing time of the shock. In case of the lowest 1σ limit on the integrated spectral index (i.e. $\alpha = -1.06$), the lower limit for the Mach number is $\mathcal{M}_{\text{G}}^{\text{int}} \geq 5.8$.

The estimate of the Mach numbers through the injection and integrated spectral indices has pros and cons, as discussed in Sec. 4.1.3 of Hoang et al. (2017). In the former method, the injection index is mostly affected by the projection effect, beside the spatial resolution and the misalignment of radio images. The measurement bias for the injection index is reduced when the shock propagates on the plane of the sky as it minimises the mixture of relativistic electrons with different spectra in the downstream region. Although the plane of shock waves in CIG0217 is unconstrained, it is unlikely to deviate significantly from the plane of the sky as it is typically found for double-relic clusters. Hence, the injection spectral indices obtained directly from the spectral index map provide more reliable estimates of the shock Mach numbers associated with the relics. Moreover, the orientation of the major axes of the relics D, F, and G suggests that they are related to a structure which is supported by the Mach numbers of these relics not being largely different (i.e. 2.0 – 2.4; Tab. 5). In the latter method, while the measurement of the integrated spectral index is not biased by the spatial resolution, the projection effect, and the misalignment of the radio images, it uses an approximation in Eq. 7 that assumes that radio relics are caused by planar shock waves. However, simulation studies by Kang (2015a,b) found that the assumption does not hold for spherical shocks that are typically found in merging systems (due to their arc-like shape). The deviation significantly increases in time as the shock propagates towards the outskirts. This explanation is in line with the fact that the radial distance increases from 1.6 Mpc, to 2.5 Mpc and 2.9 Mpc for D, F, and G, respectively. As a result, the Mach numbers estimated with the integrated spectral indices largely differ from those using the spectral index map (i.e. $\mathcal{M}_{\text{D}}^{\text{int}} = 2.6^{+0.2}_{-0.2}$ and $\mathcal{M}_{\text{F}}^{\text{int}} = 4.8^{+3.4}_{-1.0}$, but it is unusable for the extreme case of the relic G). On the other side, the Mach number discrepancy for C is more significant than that of F although the relic C is closer to the cluster centre than F. This could imply that the shocks in the W (for C) and SE (for F) directions travels through different physical environments. The discrepancy for the shock Mach numbers associated with the relics are more visible in Fig. 15 that shows a scatter plot between the Mach numbers estimated with two methods and distance of the relics from the cluster centre.

4.2.2. Shock re-acceleration of fossil electrons

For relics associated with low Mach number ($\mathcal{M} \lesssim 2.5$) shocks, the efficiency of particle acceleration directly from the thermal pool is generally high ($\eta_e > 0.1$, Botteon et al. 2020a; Brunetti & Jones 2014). However, current theoretical models predict a smaller efficiency (i.e. a few percent) for low Mach number shocks (e.g. Kang & Jones 2005; Kang & Ryu 2013). A possibility for the generation of the relics by these shocks is that the radio-emitting relativistic electrons are re-accelerated from a population of mildly relativistic electrons from, e.g., previous cluster mergers, AGN activities, or supernovae (e.g. van Weeren et al. 2013; Bonafede et al. 2014; Shimwell et al. 2015; Botteon et al. 2016; van Weeren et al. 2017). In this re-acceleration scenario, the energy that is required to dispatch in to the radio-emitting relativistic electrons by the shocks decreases. Hence, the acceleration efficiency required to produce the brightness of

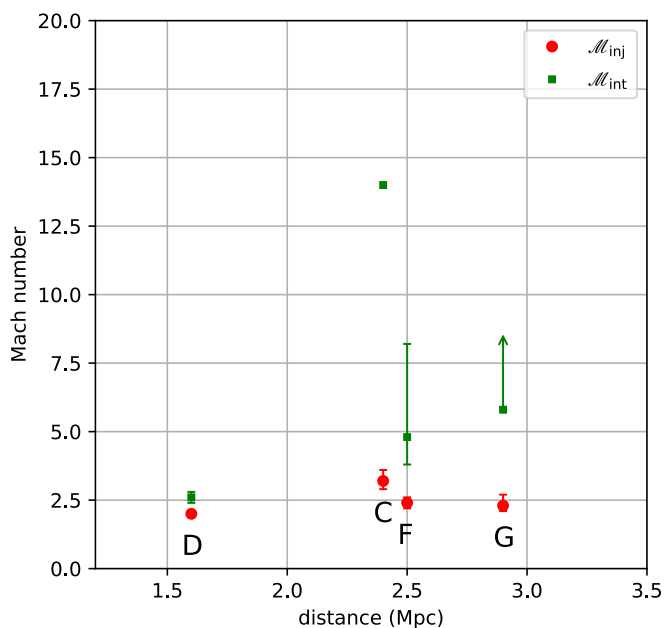


Fig. 15: A scatter plot of the shock Mach numbers and the distance of the relics from the cluster centre.

the relics is lower. In addition, unlike the thermal population that smoothly distributes over the cluster volume, fossil plasma from, e.g., AGN activities typically has small-scale structure that is similar to that of the relics (e.g. Bonafede et al. 2014).

In ClG0217, the relics, excluding C, are associated with low Mach number ($\mathcal{M} = 2.0 - 2.4$) shocks that are likely to be too weak for a direct acceleration of the thermal electrons and, as discussed, requires the presence of a population of fossil plasma prior the shock passage. Supporting evidence for this scenario in ClG0217 is that the relics show clumpy structure and extended radio emission in front of the shock fronts. Our result is in line with Brown et al. (2011) where the re-acceleration of fossil electrons by AGN activities was pointed out to explain the variations in the radio SB of the relics (C, G, and F). In addition, the location of F1 and C1 in the LOFAR maps suggests a possible connection with the relics C and F. The steep ($\alpha < -1.7$) spectral properties of C1 and F1 further support their nature being fossil plasma, rather than associating with merger shocks. However, our LOFAR observations do not detect diffuse faint emission in front of the entire length of the relics (C and F), suggesting that the radio emission of the fossil electrons in these regions is fainter which requires deeper observations to confirm.

4.3. Spectral variations over source E

To examine the spectral index in source E, we extract spectra in the square regions from the centre of the southern part towards the north (Fig. 14, *left*). The size of the regions is $16'' \times 16''$, corresponding a physical size of $49 \text{ kpc} \times 49 \text{ kpc}$. The projected distance along these 18 regions is 870 kpc. In Fig. 14 (*middle*) we present the extracted spectra from the regions. The spectral index steepens from the central region of the AGN towards the northern lobe (i.e. from -0.82 ± 0.08 in region 1 to -1.10 ± 0.15 in region 5). In the regions between the southern and northern parts of E (regions 6 – 8), the diffuse emission is undetected with the VLA 1.5 GHz, implying a steep spectral index below -1.25 . The spectral steepening feature is typically observed in

lobes of AGNs which is due to the energy losses via synchrotron and inverse-Compton radiation. Further to the northern direction the spectral index becomes flatter. The index increases up to -0.68 ± 0.11 in the regions 13 – 15 where the source is significantly brighter at 1.5 GHz (Fig. 14, *middle*).

The spectral flattening in the northern part of source E suggests the presence of a physical process that re-accelerates the fossil plasma of the southern AGN and/or amplifies the magnetic field in the regions. A possible origin of such process is caused by a merger shock that is propagating eastwards. One such example has been observed in the merging galaxy cluster Abell 3411-3412 (van Weeren et al. 2017). In this case, fossil electrons from an AGN lobe lose their energy by spectral ageing before they are re-accelerated or adiabatically compressed by a merger shock. The re-acceleration leads to the spectral flattening of the radio emission in the region of the shock front. An additional feature of the shock re-acceleration is that the spectral index also steepens in the direction behind the shock front or towards the cluster centre as for outwards moving shocks. Some other examples for the relic-AGN connection and/or interaction between AGN in shocks include the S relic of the Sausage (Genaro et al. 2018), Abell 781 (Botteon et al. 2019), the E relic of RXC J1314.4–2515 (Stuardi et al. 2019), and the NW relic of PLCK G287.0+32.9 (Bonafede et al. 2014).

To examine this possible spectral ageing behind the northern part of E of ClG0217, we extract spectra in the regions across the width of its northern part (i.e. in E–W direction; see Fig. 14). The region size in the E–W direction is equal to the resolution of the LOFAR 141 MHz and VLA 1.5 GHz images, i.e. $16''$. The spectral index profile in Fig. 14 indicates a spectral steepening from east to west (i.e. from -0.76 ± 0.12 to -1.08 ± 0.13). This spectral steepening further supports our speculation that the northern part of E is re-accelerated/compressed by an outwards moving shock. Using Eq. 6 and the spectral index of -0.76 ± 0.12 , we find that the Mach number of the possible shock is $\mathcal{M}_E = 2.9^{+1.0}_{-0.4}$. In case we use the integrated spectral index for the northern part (i.e. -1.20 ± 0.05), the corresponding Mach number is $\mathcal{M}_E^{\text{int}} = 3.3^{+0.5}_{-0.3}$ which is consistent within 1σ with the estimate directly using the spectral index map. Although the uncertainties of the Mach numbers are high, the consistency between the Mach numbers for the northern part of E might be due to the fact that the source E is closer to the cluster centre (e.g. compared with C, F, and G) where the approximation in Eq. 7 still holds. The presence of the shock front, if exists, can be confirmed by future X-ray observations that we are unable to check with the current data.

5. Conclusions

In this paper, we present LOFAR 120 – 168 MHz and VLA 1.5 GHz observations of the merging galaxy cluster ClG0217 that was previously studied with the VLA 1.4 GHz and 325 MHz by Brown et al. (2011). The LOFAR observations provide the first radio images of the cluster at the frequencies below 200 MHz and confirm the presence of a giant radio halo and multiple radio relics in the cluster. To study the nature of these diffuse sources, we made spectral index maps of the cluster using the LOFAR 141 MHz and VLA 1.4 GHz/1.5 GHz data sets. We also made use of the archival *Chandra* data to investigate the correlation between the thermal and non-thermal emission from the central radio halo and search for discontinuity in the X-ray SB. We summarise the results below.

1. The radio halo with a projected size of 1.8 Mpc is observed to be more extended at 141 MHz than that at higher frequency

- of 1.4 GHz. Its flux density at 141 MHz is 623.6 ± 62.7 mJy, corresponding to a radio power of $P_{141 \text{ MHz}} = (56.9 \pm 5.7) \times 10^{24} \text{ W Hz}^{-1}$. The radio power of CIG0217 is roughly in line with the prediction from the radio power – mass relation.
2. The non-thermal radio and thermal X-ray emission in the halo region where the radio and X-ray emission is detected above 2σ are positively correlated. At 141 MHz, the correlation is consistent with a linear relation, $\log_{10} I_R \propto b \times \log_{10} I_X$, where $b_{141 \text{ MHz}} = 1.03 \pm 0.09$. However, at 1.4 GHz the correlation follows a sub-linear relation with $b_{1.4 \text{ GHz}} = 0.81 \pm 0.06$. The results suggest that the non-thermal components at high frequencies (1.4 GHz) decline more slowly than those at low frequencies (141 MHz). This implies that there are additional non-thermal processes (particle acceleration and/or magnetic field amplification) in the outer regions of the halo as found in the X-ray data. However, our high spectral index uncertainties do not allow us to draw a firm conclusion on this as we found that the spectral index is roughly constant within a radius of 640 kpc.
 3. At 141 MHz the relics D and F are connected and are likely to belong to the same source with a projected size of 3.5 Mpc which makes this structure the largest radio relic found to date. Source G is possibly part of this structure, but deeper observations are needed to confirm this.
 4. The spectral steepening is found across the width of the relics C, D, F, and G, implying the spectral ageing of the sources. Using the spectral index at the outer edge of the relics, we found that the relics are generated by low Mach number shocks that are likely unable to directly accelerate thermal electrons to create the observed SB in the relics. An extra-source of energy with steep spectra, e.g. from fossil electrons, is required. The presence of such steep-spectrum sources, i.e. C1 and F1, in our LOFAR data supports this re-acceleration scenario.
 5. Thanks to the high-resolution images from the LOFAR 141 MHz and VLA 1.5 GHz, source E is resolved into a double lobe radio galaxy in the south and an elongated tail in the north. We found the spectral flattening in the north and suggest a possible re-acceleration by a merger shock that is moving outwards in the northern region of E.

The late stage merging galaxy cluster CIG0217 is a dynamically rich system that hosts multiple radio relics and a giant radio halo. These extended radio sources are ideal locations for studying particle (re-)acceleration, turbulence and magnetic field amplification in the late stage of cluster merger. Our study using multi-wavelength data sets provide new insights into the nature of the sources (i.e. classification, morphology, spectral properties, and interplay between thermal and non-thermal components). However, due to the quality of the current data, we are unable to confirm some aspects associated with, e.g., radio spectral emission at the X-ray discontinuities in the halo, spectral flattening in the north of source E, and the presence of shock fronts at the location of the relics. Further study using multi-wavelength (radio, X-ray, optical) observations will be necessary to further investigate these.

Acknowledgements. DNH and AB acknowledge support from the ERC through the grant ERC-Stg DRANOEL n. 714245. MB acknowledges support from the Deutsche Forschungsgemeinschaft under Germany's Excellence Strategy - EXC 2121 "Quantum Universe" - 390833306. XZ acknowledges support from China Scholarship Council. SRON is supported financially by NWO, The Netherlands Organisation for Scientific Research. RJvW acknowledges support from the ERC Starting Grant ClusterWeb 804208. AB acknowledges support from the VIDI research programme with project number 639.042.729, which is financed by the Netherlands Organisation for Scientific Research (NWO). AS is supported

by the Women In Science Excel (WISE) programme of the Netherlands Organisation for Scientific Research (NWO), and acknowledges the World Premier Research Center Initiative (WPI) and the Kavli IPMU for the continued hospitality. SRON Netherlands Institute for Space Research is supported financially by NWO. GB acknowledges partial support from INAF mainstream program "Galaxy clusters science with LOFAR" LOFAR (van Haarlem et al. 2013) is the Low Frequency Array designed and constructed by ASTRON. It has observing, data processing, and data storage facilities in several countries, which are owned by various parties (each with their own funding sources), and that are collectively operated by the ILT foundation under a joint scientific policy. The ILT resources have benefited from the following recent major funding sources: CNRS-INSU, Observatoire de Paris and Université d'Orléans, France; BMBF, MIWF-NRW, MPG, Germany; Science Foundation Ireland (SFI), Department of Business, Enterprise and Innovation (DBEI), Ireland; NWO, The Netherlands; The Science and Technology Facilities Council, UK; Ministry of Science and Higher Education, Poland; The Istituto Nazionale di Astrofisica (INAF), Italy. This research made use of the Dutch national e-infrastructure with support of the SURF Cooperative (e-infra 180169) and the LOFAR e-infra group. The Jülich LOFAR Long Term Archive and the German LOFAR network are both coordinated and operated by the Jülich Supercomputing Centre (JSC), and computing resources on the supercomputer JUWELS at JSC were provided by the Gauss Centre for Supercomputing e.V. (grant CHTB00) through the John von Neumann Institute for Computing (NIC). This research made use of the University of Hertfordshire high-performance computing facility and the LOFAR-UK computing facility located at the University of Hertfordshire and supported by STFC [ST/P000096/1], and of the Italian LOFAR IT computing infrastructure supported and operated by INAF, and by the Physics Department of Turin university (under an agreement with Consorzio Interuniversitario per la Fisica Spaziale) at the C3S Supercomputing Centre, Italy. The scientific results reported in this article are based on data obtained from the *Chandra* Data Archive. This research has made use of software provided by the *Chandra* X-ray Center (CXC) in the application packages CIAO, ChIPS, and Sherpa. The National Radio Astronomy Observatory is a facility of the National Science Foundation operated under cooperative agreement by Associated Universities, Inc.

References

- Alam, S., Albareti, F. D., Prieto, C. A., et al. 2015, *Astrophys. Journal*, Suppl. Ser., 219
- Arnaud, M., Pointecouteau, E., & Pratt, G. W. 2007, *A&A*, 474, L37
- Bell, A. R. & R., A. 1978, *MNRAS*, 182, 147
- Blandford, R. & Eichler, D. 1987, *Phys. Rep.*, 154, 1
- Bonafede, A., Intema, H. T., Brüggén, M., et al. 2014, *ApJ*, 785, 1
- Botteon, A., Brunetti, G., Ryu, D., & Roh, S. 2020a, *A&A*, 634, A64
- Botteon, A., Brunetti, G., van Weeren, R. J., et al. 2020b, *ApJ*, 897, 93
- Botteon, A., Gastaldello, F., Brunetti, G., & Dallacasa, D. 2016, *Mon. Not. R. Astron. Soc. Lett.*, 460, L84
- Botteon, A., Shimwell, T. W., Bonafede, A., et al. 2019, *A&A*, 622, A19
- Boxelaar, J. M., van Weeren, R. J., & Botteon, A. 2021, (submitted) [arXiv:2103.08554]
- Brown, S., Duisterhoef, J., & Rudnick, L. 2011, *ApJ*, 727, L25
- Brown, S. & Rudnick, L. 2011, *MNRAS*, 412, 2
- Brunetti, G., Cassano, R., Dolag, K., & Setti, G. 2009, *A&A*, 507, 661
- Brunetti, G. & Jones, T. W. 2014, *Int. J. Mod. Phys. D*, 23, 1430007
- Brunetti, G. & Lazarian, A. 2007, *MNRAS*, 378, 245
- Brunetti, G. & Lazarian, A. 2011, *MNRAS*, 410, 127
- Brunetti, G. & Lazarian, A. 2016, *MNRAS*, 458, 2584
- Brunetti, G., Setti, G., Feretti, L., & Giovannini, G. 2001, *MNRAS*, 320, 365
- Bruno, L., Rajpurohit, K., Brunetti, G., et al. 2021, *ArXiv e-prints*, 1
- Cassano, R., Brunetti, G., & Setti, G. 2006, *MNRAS*, 369, 1577
- Chambers, K. C., Magnier, E. A., Metcalfe, N., et al. 2019, *ArXiv e-prints* [arXiv:1612.05560]
- de Gasperin, F., Brunetti, G., Brüggén, M., et al. 2020, *arXiv*, 15, 1
- de Gasperin, F., Dijkema, T. J., Drabent, A., et al. 2019, *A&A*, 622, A5
- Delain, K. M. & Rudnick, L. 2006, *Astron. Nachrichten*, 327, 561
- Drury, L. O. 1983, *Reports Prog. Phys.*, 46, 973
- Enßlin, T. A., Biermann, P. L. P., Klein, U., et al. 1998, *A&A*, 409, 395
- Feretti, L., Fusco-Femiano, R., Giovannini, G., & Govoni, F. 2001, *\aap*, 373, 106
- Feretti, L., Orru, E., Brunetti, G., et al. 2004, *A&A*, 423, 111
- Foreman-Mackey, D., Hogg, D. W., Lang, D., & Goodman, J. 2013, *Publ. Astron. Soc. Pacific*, 125, 306
- Gennaro, G. D., van Weeren, R. J., Hoeft, M., et al. 2018, *ApJ*, 865, 24
- Ginzburg, V. & Syrovatskii, S. 1969, *The origin of cosmic rays* (New York: Gordon and Breach)
- Giovannini, G., Feretti, L., Venturi, T., Kim, K.-T., & Kronberg, P. P. 1993, *ApJ*, 406, 399

- Govoni, F., Enßlin, T. A., Feretti, L., & Giovannini, G. 2001a, *A&A*, 369, 441
- Govoni, F., Feretti, L., Giovannini, G., et al. 2001b, *A&A*, 819, 803
- Haarlem, M. P. V., Wise, M. W., Gunst, A. W., et al. 2013, *A&A*, 2, 1
- Hoang, D. N., Shimwell, T. W., Stroe, A., et al. 2017, *MNRAS*, 471, 1107
- Hoang, D. N., Shimwell, T. W., van Weeren, R. J., et al. 2019a, *A&A*, 622, A20
- Hoang, D. N., Shimwell, T. W., van Weeren, R. J., et al. 2018, *MNRAS*, 478, 2218
- Hoang, D. N., Shimwell, T. W., Van Weeren, R. J., et al. 2019b, *A&A*, 622, 1
- Hoefl, M., Brüggen, M., Brüggen, M., & Brüggen, M. 2007, *MNRAS*, 375, 77
- Intema, H. T., Jagannathan, P., Mooley, K. P., & Frail, D. A. 2017, *A&A*, 598, A78
- Kang, H. 2015a, *J. Korean Astron. Soc.*, 48, 9
- Kang, H. 2015b, *J. Korean Astron. Soc.*, 48, 155
- Kang, H. & Jones, T. W. 2005, *ApJ*, 620, 44
- Kang, H. & Ryu, D. 2011, *ApJ*, 734, 18
- Kang, H. & Ryu, D. 2013, *ApJ*, 764, 95
- Kang, H., Ryu, D., & Jones, T. W. 2012, *ApJ*, 756, 97
- Kelly, B. C. 2007, *ApJ*, 665, 1489
- Liang, H., Hunstead, R. W., Birkinshaw, M., & Andreani, P. 2000, *ApJ*, 544, 686
- Markevitch, M., Govoni, F., Brunetti, G., & Jerius, D. 2005, *ApJ*, 627, 733
- Markevitch, M. & Vikhlinin, A. 2007, *Phys. Rep.*, 443, 1
- McMullin, J., Waters, B., Schiebel, D., Young, W., & Golap, K. 2007, in *Astronomical Society of the Pacific Conference Series*, Vol. 376, *Astron. Data Anal. Softw. Syst. XVI*, ed. R. Shaw, F. Hill, & D. Bell, 127
- Murgia, M., Govoni, F., Markevitch, M., et al. 2009, *A&A*, 499, 679
- Offringa, A. R., McKinley, B., Hurley-Walker, N., et al. 2014, *MNRAS*, 444, 606
- Offringa, R. & Smirnov, O. 2017, *MNRAS*, 16, 1
- Orrù, E., Murgia, M., Feretti, L., et al. 2007, *A&A*, 467, 943
- Owers, M. S., Nulsen, P. E., Couch, W. J., & Markevitch, M. 2009, *ApJ*, 704, 1349
- Pearce, C. J. J., van Weeren, R. J., Andrade-Santos, F., et al. 2017, *ApJ*, 845, 81
- Perley, R. A. & Butler, B. J. 2017, *Astrophys. J. Suppl. Ser.*, 230, 7
- Petrosian, V. 2001, *ApJ*, 557, 560
- Pinzke, A., Oh, S. P., & Pfrommer, C. 2017, *MNRAS*, 465, 4800
- Rajpurohit, K., Brunetti, G., Bonafede, A., et al. 2021, *A&A*, 646, A135
- Rajpurohit, K., Hoefl, M., van Weeren, R. J., et al. 2018, *ApJ*, 852, 65
- Rajpurohit, K., Hoefl, M., Vazza, F., et al. 2020, *A&A*, 636, A30
- Rengelink, R. B., Tang, Y., de Bruyn, A. G., et al. 1997, *Astron. Astrophys. Suppl. Ser.*, 124, 259
- Roettiger, K., Burns, J. O., & Stone, J. M. 1999, *ApJ*, 518, 603
- Rudnick, L., Delain, K. M., & Lemmerman, J. A. 2006, *Astron. Nachrichten*, 327, 549
- Sarazin, C. L. C. C. L. 2002, *Springer*, 272, 1
- Shimwell, T. W., Brown, S., Feain, I. J., et al. 2014, *MNRAS*, 440, 2901
- Shimwell, T. W., Markevitch, M., Brown, S., et al. 2015, *MNRAS*, 449, 1486
- Shimwell, T. W., Röttgering, H. J. A., Best, P. N., et al. 2017, *A&A*, 598, A104
- Shimwell, T. W., Tasse, C., Hardcastle, M. J., et al. 2019, *A&A*, 622, A1
- Stroe, A., van Weeren, R. J., Intema, H. T., et al. 2013, *A&A*, 555, A110
- Stuardi, C., Bonafede, A., Wittor, D., et al. 2019, *MNRAS*, 489, 3905
- Tasse, C., Shimwell, T., Hardcastle, M. J., et al. 2021, *A&A*, 648, A1
- van Weeren, R. J., Andrade-Santos, F., Dawson, W. A., et al. 2017, *Nat. Astron.*, 1, 5
- van Weeren, R. J., Brunetti, G., Brüggen, M., et al. 2016a, *ApJ*, 818, 204
- van Weeren, R. J., de Gasperin, F., Akamatsu, H., et al. 2019, *Space Sci. Rev.*, 215, 16
- van Weeren, R. J., Fogarty, K., Jones, C., et al. 2013, *ApJ*, 769, 101
- van Weeren, R. J., Shimwell, T. W., Botteon, A., et al. 2020, *ArXiv e-prints* [[arXiv:2011.02387](https://arxiv.org/abs/2011.02387)]
- van Weeren, R. J., Williams, W. L., Hardcastle, M. J., et al. 2016b, *Astrophys. J. Suppl. Ser.*, 223, 2
- Vazza, F. & Brüggen, M. 2014, *MNRAS*, 437, 2291
- Zhang, X., Simionescu, A., Kaastra, J. S., et al. 2020, *A&A*, 642, L3

Appendix A: Spectral index error maps

The spectral index maps for CIG0217 are shown in Fig. A.1.

Appendix B: Optical images

In Fig. B.1 we present cutout optical images in the regions of radio sources.

Appendix C: Fitting the radio halo with a circular 2D model.

The maximum likelihood parameters and the uncertainties are estimated using the `code` (Foreman-Mackey et al. 2013). The corner plots for the fitting parameters with elliptical exponential 2D model are shown in Fig. C.1.

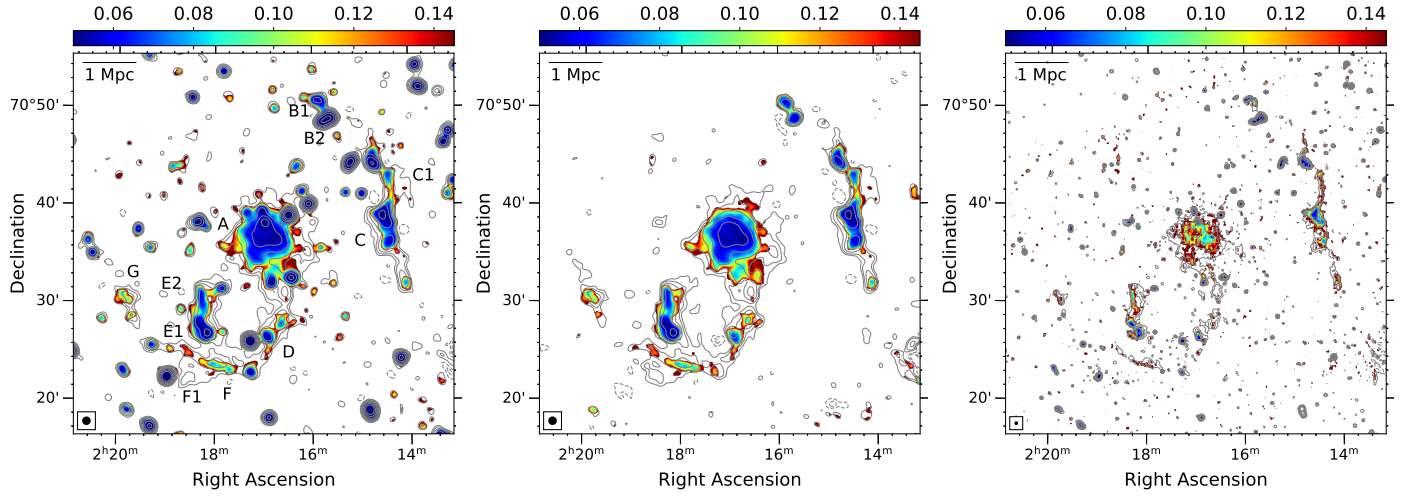


Fig. A.1: Spectral index error maps at low (*left* and *middle*) and high (*right*) resolutions. The *middle* image has point sources subtracted.

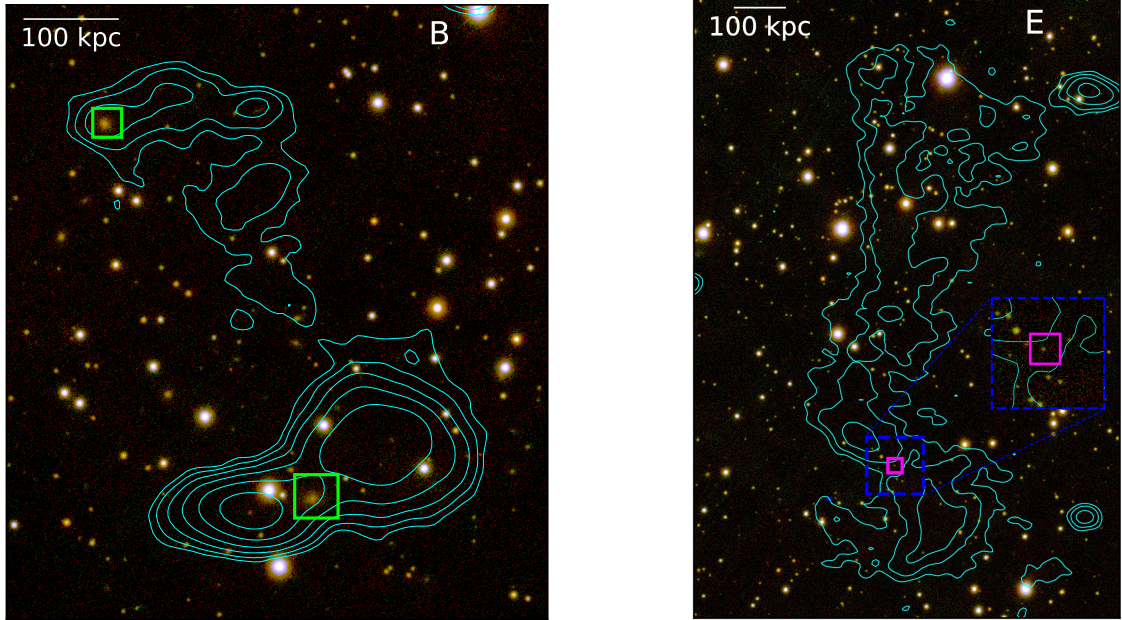


Fig. B.1: Pan-STARRS color (y, i, g) image of sources B (*left*) and E (*right*). The square magenta regions show the optical counterparts of the radio galaxies.

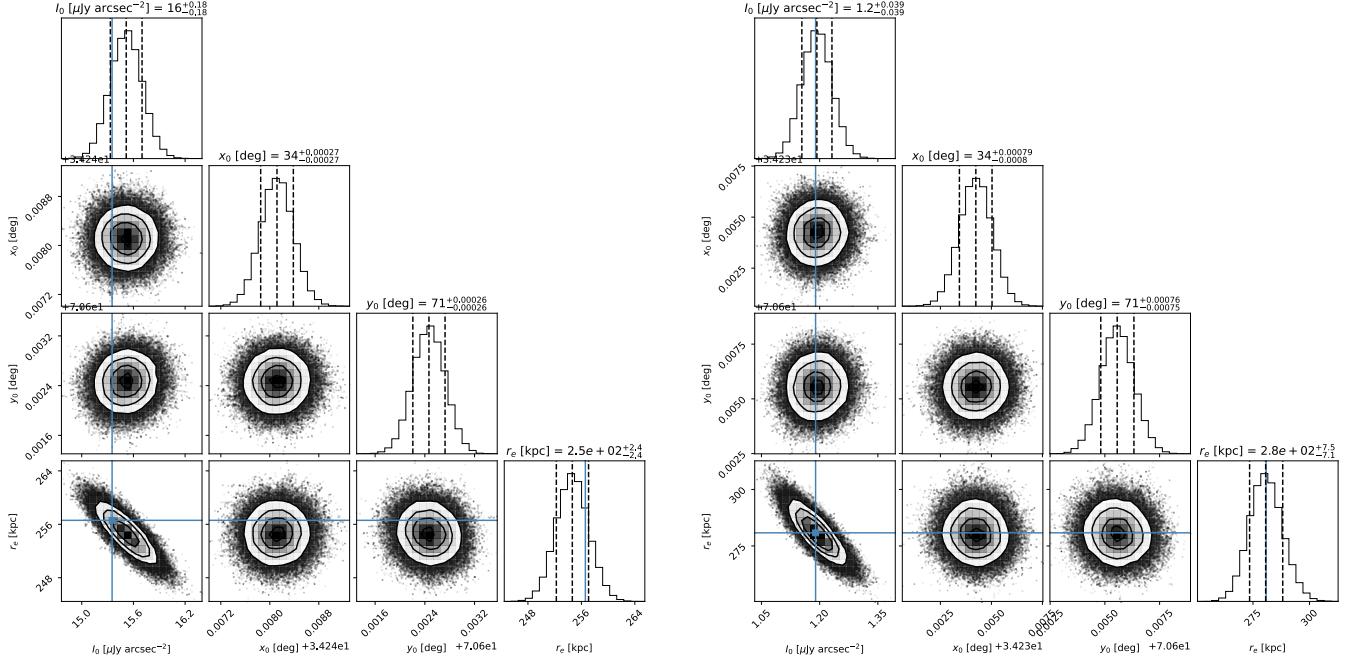


Fig. C.1: Corner plots obtained from the fitting of a 2D circular model to the SB of the radio halo at 141 MHz (*left*) and 1.4 GHz (*right*).